

THE INITIAL CONDITIONS AND EVOLUTION OF ISOLATED GALAXY MODELS: EFFECTS OF THE HOT GAS HALO

JEONG-SUN HWANG¹, CHANGBOM PARK¹, & JUN-HWAN CHOI²

¹ School of Physics, Korea Institute for Advanced Study, Heogiro 85, Seoul 130-722, Korea

²Department of Physics and Astronomy, University of Kentucky, Lexington, KY, 40506-0055, U.S.A.; jhchoi@pa.uky.edu

Draft version October 30, 2018

ABSTRACT

We construct several Milky Way-like galaxy models containing a gas halo (as well as gaseous and stellar disks, a dark matter halo, and a stellar bulge) following either an isothermal or an NFW density profile with varying mass and initial spin. In addition, galactic winds associated with star formation are tested in some of the simulations. We evolve these isolated galaxy models using the GADGET-3 N -body/hydrodynamic simulation code, paying particular attention to the effects of the gaseous halo on the evolution. We find that the evolution of the models is strongly affected by the adopted gas halo component, particularly in the gas dissipation and the star formation activity in the disk. The model without a gas halo shows an increasing star formation rate (SFR) at the beginning of the simulation for some hundreds of millions of years and then a continuously decreasing rate to the end of the run at 3 Gyr. Whereas the SFRs in the models with a gas halo, depending on the density profile and the total mass of the gas halo, emerge to be either relatively flat throughout the simulations or increasing until the middle of the run over a gigayear, then decreasing to the end. The models with the more centrally concentrated NFW gas halo show overall higher SFRs than those with the isothermal gas halo of the equal mass. The gas accretion from the halo onto the disk also occurs more in the models with the NFW gas halo, however, this is shown to take place mostly in the inner part of the disk and not to contribute significantly to the star formation unless the gas halo has very high density at the central part. The rotation of a gas halo is found to make SFR lower in the model. The SFRs in the runs including galactic winds are found to be lower than the same runs but without winds. We conclude that the effects of a hot gaseous halo on the evolution of galaxies are generally too significant to be simply ignored. We also expect that more hydrodynamical processes in galaxies could be understood through numerical simulations employing both gas disk and gas halo components.

Subject headings: methods: numerical — galaxies: evolution — galaxies: spiral — galaxies: halos — galaxies: structure — galaxies: star formation

1. INTRODUCTION

Under the hierarchical galaxy formation scenario, galaxy interactions play a key role in the evolution of galaxies (e.g. Toomre & Toomre 1972; Barnes & Hernquist 1992). Owing to the nonlinear nature of the galaxy interactions, theoretical studies mostly rely on N -body/hydrodynamic simulations. The initial conditions of the simulations often adopt isolated galaxy models. Galaxy models in many galaxy interaction simulations include dark matter halo, gas disk, stellar disk, and stellar bulge (Hernquist 1993; Springel et al. 2005). Unfortunately, generating an isolated stable galaxy model is not trivial procedure. It is required to solve complicated orbit integrations to make stable stellar systems (Osipkov 1979; Merritt 1985; Kazantzidis et al. 2004). The interactions among the different components significantly modify the very initial setups (Blumenthal et al. 1984). Furthermore, it is needed to satisfy the initially hydrostatic condition of the gas components. In order to isolate the galaxy interaction effects, it is necessary to carefully build the initial galaxy model and understand the evolution of the initial conditions, if there are any. However, the basic steps to construct various types of initial galaxy models are often omitted or discussed

shortly. The detailed comparison studies of the evolution of different galaxy models in isolation are also not found sufficiently in the literature.

Moreover, it has been reported that some spiral galaxies like our own Milky Way as well as elliptical galaxies possess hot diffuse gas in the halo. Importance of hot halo gas in the evolution of galaxies has been also evidenced by Park et al. (2008), Park & Choi (2009), Park & Hwang (2009), and Hwang & Park (2009) who studied the effects of galaxy interactions on galaxy properties such as morphology, color, and star formation activity among others at various environment and redshifts. It has been consistently suggested by these studies that the hydrodynamic interaction between galaxies through exchange of cold gas and/or impact of hot halo gas makes a crucial role in the evolution of galaxy color and star formation activity. However, only a few numerical studies taking account of halo gas in the models have been presented. Recently, Moster et al. (2011) performed hydrodynamic simulations of major mergers of disk galaxies, including for the first time a gradually cooling hot gas halo in their galaxy models. They studied the impact of a gaseous halo and galactic winds on the star formation activity during mergers and found that the gas halo component strongly affects the kinematics and internal structure of the merger remnants as well as the star for-

mation history on the course of the merger. In a follow-up study (Moster et al. 2012), they also investigated the role of a hot gas component on disk thickening during minor merger and showed the dependency of the final scale height on the mass of the hot halo, the efficiency of the winds, and the merger mass ratio. They found that the cooling of the hot gaseous halo regenerates the thin disk, so that the remnants of 1:10 mergers exhibit a newly formed thin disk. These findings suggest that the existence of a hot gaseous halo significantly affects the results of galaxy interactions. It may be necessary to reinterpret many previous galactic scale simulation results that did not consider a hot gaseous halo.

In this paper, we present detailed descriptions of the various choices of the isolated Milky Way-like galaxy models. We also study the effects of the gas halo component with different properties, such as the cumulative mass profile, total mass, and rotation of the gas halo on their evolution. This paper is the first in a series of the galaxy interaction study that includes a hot gas halo in the initial galaxy model with a hope to explain the observational studies by Park et al. (2008), Park & Choi (2009), Park & Hwang (2009), Hwang & Park (2009), and Deng et al. (2012).

Recent galaxy formation studies suggest that the galactic outflow is an essential mechanism for balance between gas accretion and galaxy growth (e.g. Dekel & Silk 1986; Springel & Hernquist 2003; Choi & Nagamine 2011; Hopkins et al. 2011). It also regulates the star formation rate of galaxies. In our study, we also include galactic outflow driven by supernovae with different wind parameters to study the effects of a gas halo and galactic winds on the evolution of isolated galaxies.

In Sec. 2, we give a brief account of the ZENO software package and explain our galaxy models and their initial parameters. We describe in Sec. 3 the simulation code GADGET-3 and the results of evolution of the models. Finally, we summarize and discuss our main results in Sec. 4. The step-by-step procedure of constructing our galaxy models is presented in Appendix A, and the long-term evolution of one of our models in Appendix B.

2. GALAXY MODELS

2.1. Numerical Code

To generate the initial galaxy models, we use the ZENO software package (version 008). ZENO is a collection of programs for N -body/SPH simulations and analysis, provided by J. E. Barnes¹.

ZENO allows one to build multiple spherical and disk components in mutual equilibrium with user-specified density profiles in collisionless or gaseous form, that fulfills our needs for constructing various galaxy models. We use about a dozen programs in the ZENO package to complete our multi-component galaxy models. The procedure of constructing the models using those programs is described in Appendix A in detail.

The ZENO programs use dimensionless units with Newton's constant $G = 1$. We set the total disk mass (including both stars and gas) as the unit mass and the radial scale length of the stellar disk as the unit length in all models. We set the components of our models to

follow those of the Milky Way Galaxy, and the units of length, mass, and time are 3.5 kpc, $5 \times 10^{10} M_\odot$, and 14 Myr, respectively. The unit velocity then corresponds to 247 km s⁻¹.

2.2. Density Profiles

In our models both star and gas disks have an exponential surface density profile and a sech² vertical profile (c.f. Barnes & Hibbard 2009):

$$\rho_{dc}(R, z) = \frac{M_{dc}}{4\pi a_{dc}^2 z_{dc}} e^{-R/a_{dc}} \text{sech}^2\left(\frac{z}{z_{dc}}\right), \quad (1)$$

where 'c' stands for either 's' for the star disk component or 'g' for the gas disk component. R is the cylindrical radius $R = (x^2 + y^2)^{1/2}$ and M_{dc} is the mass of the star or the gas disk. a_{dc} is the radial scale length and z_{dc} is the vertical scale height of the disk. A few distant particles farther than a cut-off radius (b_{dc}) are removed. The gas disk is radially more extended than the star disk in our models. The radial and vertical scales of the gas disk are chosen as $a_{dg} = 2.5 \times a_{ds}$ and $z_{dg} = z_{ds}$.

The mass density of the DM halo of all models and the gas halo of some models follows an NFW profile (Navarro et al. 1996). Since the cumulative mass of the profile diverges at large radii, an exponential taper is applied at radii larger than b_{hc} :

$$\rho_{hc}(r) = \begin{cases} \frac{M_{hc}(a_{hc})}{4\pi(\ln(2) - \frac{1}{2})} \frac{1}{r(r + a_{hc})^2} & \text{for } r \leq b_{hc}, \\ \rho_{hc}^* \left(\frac{b_{hc}}{r}\right)^2 e^{-2\beta(r/b_{hc}-1)} & \text{for } r > b_{hc}, \end{cases} \quad (2)$$

where 'c' represents either 'd' for the DM halo component or 'g' for the gas halo component. a_{hc} is the radial scale of the DM or gas halo model and $M_{hc}(a_{hc})$ is the mass of the halo within a_{hc} . The radial scales of both DM and gas halos are chosen to be the same. ρ_{hc}^* and β are calculated by requiring both $\rho_{hc}(r)$ and $d\rho_{hc}/dr$ to be continuous at b_{hc} .

The gas halo of the rest of our models follows a non-singular isothermal profiles with truncation:

$$\rho_{hg}(r) = \frac{f_{\text{norm}} M_{hg}}{2\pi\sqrt{\pi} b_{hg}} \frac{1}{r^2 + a_{hg}^2} e^{-(r/b_{hg})^2}, \quad (3)$$

where a_{hg} and b_{hg} are the radius of core and taper, respectively. f_{norm} is a function of a_{hg} and b_{hg} , and M_{hg} is the total mass of the halo gas.

The mass density of the bulge, which consists of stars only, in all models follows a Hernquist (1990) profile, with a cut-off at large radii for efficient computation:

$$\rho_b(r) = \begin{cases} \frac{a_b M_b}{2\pi} \frac{1}{r(a_b + r)^3} & \text{for } r \leq b_b, \\ \rho_b^* \left(\frac{b_b}{r}\right)^2 e^{-2r/b_b} & \text{for } r > b_b, \end{cases} \quad (4)$$

where a_b is the radial scale of the bulge model and b_b is the radius at which truncation starts. M_b is the mass of the bulge. ρ_b^* is determined by the continuity of $\rho_b(r)$ at $r = b_b$. For $b_b \gg a_b$, $d\rho_b/dr$ is continuous at $r = b_b$ as well.

¹ <http://www.ifa.hawaii.edu/~barnes/software.html>

2.3. Initial Galaxy Models

We construct seven different galaxy models in total. Their basic properties are summarized in Tables 1 and 2. We first build model DHi as our fiducial model. It contains a gas halo component following an isothermal density profile. We then generate six more comparison models without or with a gas halo of varying properties.

Our models are characterized by the existence of a gas halo and denoted by initials DH, D, and H. (D and H stand for disk and halo, respectively.): The models of type DH, such as the fiducial model DHi, consist of three collisionless components, dark matter (DM) halo, stellar disk, and stellar bulge, as well as two gaseous components, gas halo and gas disk. The models of types D and H also possess the three collisionless components but have only one gaseous component at the initial time, either gas disk in type D or gas halo in type H.

In all types of our models, the total mass is set to $M_{\text{tot}} = 126 \times 10^{10} M_{\odot}$, i.e., as similarly massive as the Milky Way Galaxy. The total masses of the halo (DM + gas, if the model includes a gas halo), the disk (stars + gas, if the model has a gas disk), and the bulge (stars only) components are $M_{\text{h}} = M_{\text{hd}} + M_{\text{hg}} = 120 \times 10^{10} M_{\odot}$, $M_{\text{d}} = M_{\text{ds}} + M_{\text{dg}} = 5 \times 10^{10} M_{\odot}$, and $M_{\text{b}} = 1 \times 10^{10} M_{\odot}$, respectively in all models.

We test two different cumulative mass profiles for the gas halo, the isothermal density profile (Eq. 3) and the NFW profile (Eq. 2). According to the adopted mass profile, the models of type DH are divided into two subtypes - DHi and DHn. The gas halo of the models of subtype DHi (models DHi, DHi-f5, and DHir) and model Hi follows the isothermal profile, and that of subtype DHn (models DHn and DHn-f5) follows the NFW profile.

We also try two distinct values of halo gas fraction $f_{\text{hg}} = M_{\text{hg}}/M_{\text{h}}$ (Table 1), in order to examine how galaxy models with different amounts of hot gas evolve differently. In one case, the halo gas fraction in models DHi, DHir, DHn, and Hi (without ‘-f5’ in the model names) is chosen to be $f_{\text{hg}} = 0.01$, which corresponds to $M_{\text{hg}} = 1.2 \times 10^{10} M_{\odot}$. This mass of a gaseous halo is motivated from Anderson & Bregman (2010) where the upper limit of the hot halo mass of the Milky Way Galaxy is estimated to be $< 1.2 - 1.5 \times 10^{10} M_{\odot}$ from the observed dispersion measure of pulsars in the Large Magellanic Cloud, assuming an NFW profile for the hot gas. In the other case, in models DHi-f5 and DHn-f5, a more massive gas halo with $f_{\text{hg}} = 0.05$ is adopted, which corresponds to $M_{\text{hg}} = 6 \times 10^{10} M_{\odot}$. The more massive gas halo is motivated from Moster et al. 2011. In their model with the maximum hot gas fraction, the mass of the gas halo within the virial radius is $M_{\text{hg}} = 1.2 \times 10^{11} M_{\odot}$, such that the baryonic fraction within the virial radius has the universal value.

The gas fraction in the disk is chosen to be a single value of $f_{\text{dg}} = M_{\text{dg}}/M_{\text{d}} = 0.12$ and thus $M_{\text{dg}} = 0.6 \times 10^{10} M_{\odot}$ in all models possessing a gas disk. So the total mass of cold gas in a disk is either half (in models DHi, DHir, and DHn) or a tenth (in models DHi-f5 and DHn-f5) of the total mass of the hot halo gas.

The effects of the rotation of the hot gas halo is also examined by comparing models DHi and DHir; the latter is made from the former by adding an initial spin to

the gas halo in such a way that the gas halo has the rotation curve similar to that of the gas disk, but with about half the amplitude (rotational velocity). The hot gas particles in model DHir thus have non-zero initial velocities in x and y directions but zero in z direction; in all other models with a gas halo, halo gas particles have zero initial velocities in all three directions.

The initial temperatures of the disk gas particles in all models possessing a gas disk are set to the single value of $10000 K$. The temperatures of the halo gas particles are determined by the hydrostatic equilibrium in the ZENO code (Appendix A). The gas temperature in the central part of our models within $r = 10$ kpc generally has a value between $10^6 K$ and $10^7 K$.

We summarize the key properties of each initial galaxy model below.

2.3.1. Model DHi

Model DHi is the fiducial model. As noted earlier, it consists of five components: star disk, gas disk, DM halo, gas halo, and bulge. The total mass of each of the components in the unit of $10^{10} M_{\odot}$ are $M_{\text{ds}} = 4.4$, $M_{\text{dg}} = 0.6$, $M_{\text{hd}} = 118.8$, $M_{\text{hg}} = 1.2$, and $M_{\text{b}} = 1$ as summarized in Table 2. Hence, the mass of the hot gas initialized in the halo is twice that of the cold gas in the disk. In terms of gas fractions in the disk and the halo, $f_{\text{dg}} = 0.12$ and $f_{\text{hg}} = 0.01$ as indicated in Table 1. The number of star or gas particles set in each component is $N_{\text{ds}} = 16384$, $N_{\text{dg}} = 16384$, $N_{\text{hd}} = 163840$, $N_{\text{hg}} = 32768$, and $N_{\text{b}} = 8192$. The number of gas particles in the halo is twice of that in the disk, making the same mass per gas particle in the system. The particle mass is different for different components. To minimize the effects of the mass difference of simulation particles we set $f_i \propto m_i/\epsilon_i^2$ to be equal for particles in each component, where f_i is the maximum acceleration experienced by a particle. We choose the gravitational softening length for the DM halo particles to $\epsilon_{\text{hd}} = 1$ kpc (in all models; Table 2). Then the smoothing lengths for the gas, disk star, and bulge particles are determined to be 0.225, 0.609, and 0.410 kpc, respectively.

The initial distribution of the star and gas particles and some basic profiles of the components are shown in Figs 1 and 2, respectively. As for both star and gas disks, the particle distributions in the x - y and x - z projections are presented in the first two columns of Fig. 1, and their surface density profiles in the top-left panel of Fig. 2. Both disks have the exponential surface density profile (Eq. 1). The gas disk is seen more extended than the stellar one, with the larger radial scale length of $a_{\text{dg}} = 2.5 \times a_{\text{ds}} = 8.75$ kpc (Table 2). The particle distributions of the three spheroidal components are shown in the third to fifth columns in Fig. 1, and the spherically averaged accumulated density profiles are plotted in the top-right panel of Fig. 2. The DM halo follows the NFW profile with the exponential taper (Eq. 2). The radial scale is set to $a_{\text{hd}} = 21$ kpc, the same as in the galaxy model of McMillan & Dehnen (2007), and the radius to begin taper to $b_{\text{hd}} = 84$ kpc. The mass of the DM halo within $r = a_{\text{hd}}$ is set to $M_{\text{hd}}(a_{\text{hd}}) = 12.23 \times 10^{10} M_{\odot}$ so that the total mass of the DM halo becomes $M_{\text{hd}} = 118.8 \times 10^{10} M_{\odot}$. The gas halo has the truncated isothermal profile (Eq. 3), with the core radius $a_{\text{hg}} = 10.5$ kpc and the taper radius

TABLE 1
INITIAL GALAXY MODELS

Model name	Gas halo model	Gas halo rotation	f_{hg}^{a}	f_{dg}^{b}
DHi	isothermal	...	0.01	0.12
DHi-f5	isothermal	...	0.05	0.12
DHir	isothermal	gas disk rotation $\times 0.5$	0.01	0.12
DHn	NFW	...	0.01	0.12
DHn-f5	NFW	...	0.05	0.12
D	0.12
Hi	isothermal	...	0.01	...

^a The halo gas fraction $f_{\text{hg}} = M_{\text{hg}}/M_{\text{h}}$

^b The disk gas fraction $f_{\text{dg}} = M_{\text{dg}}/M_{\text{d}}$

$b_{\text{hg}} = 420$ kpc. The choice of the core radius is motivated by the recent model of Moster et al. (2011). Given the core radius, the gas halo has nearly flat density within a_{hg} , as seen in the magenta line in the top-right panel of Fig. 2. The bulge follows the Hernquist profile with a truncation (Eq. 4). The length scale of the bulge is set to $a_{\text{b}} = 0.7$ kpc, adopted from McMillan and Dehnen (2007).

The cylindrically averaged tangential velocities $v_{\text{t}} = (v_x^2 + v_y^2)^{1/2}$ of all components with respect to R are shown in the bottom-left panel of Fig. 2. The gas disk particles are initially given to have the local circular velocities (cyan solid line) in clockwise direction with zero vertical motion ($v_z = 0$), the star disk particles to have additional dispersions (black dashed line). Note that the gas halo particles of this model are set with zero initial velocities in all three directions.

The temperature T as a function of the local gas density ρ_{local} in the disk or halo is presented in the bottom-right panel of Fig. 2. (The temperature is converted from the specific internal energy u of the gas particles, assuming that T below 10000 K, a mean molecular weight corresponding to neutral gas of primordial abundance, otherwise full ionization.) The temperature of the disk gas particles are set uniformly to $T = 10000$ K (cyan dots). The temperature of the halo gas varies (magenta dots) to achieve hydrostatic equilibrium of the hot halo gas. Those halo gas particles in the T - ρ_{local} diagram appear well-separated from the cold disk gas at the initial time. As the system evolves (the model evolution is discussed in Sec. 3), T and ρ_{local} of the gas particles will be redistributed and some of the halo and the disk particles will be mixed. For example, some cold gas particles which are originally set as the disk gas can be heated and have physical characteristics of the halo gas, and vice versa. Therefore, we establish a simple criterion, shown by the black line in the T - ρ_{local} plane, to determine if a gas particle at a certain time should be considered as the disk or the halo particle. The criterion is fixed in all our models at all times (c.f. Fig. 3). The criterion is originally set in the u - ρ_{local} plane and is converted on the assumption described above. The line is chosen such that (1) the disk and the halo gas particles of all initial galaxy models can be well-separated by the common line, (2) all disk gas particles in the model without a gas halo and without considering winds can stay below the line at all times,

(3) and all halo gas particles in the model without a gas disk and without winds can always stay above the line. Any gas particles lie below the black line at a time are considered as the disk gas and those above the line as the halo gas particles, with their origin identified by cyan or magenta in the T - ρ_{local} plot.

2.3.2. Model DHi-f5

This model is intended to have a more massive gas halo than that of the fiducial model DHi, with the other properties in common (Tables 1 and 2; to keep the total mass of the DM + gas halo the same, the DM halo of model DHi-f5 is set to be lighter than that of model DHi by the mass difference in the gas halos). Specifically, the gas halo of this model follows the same truncated isothermal density profile of Eq. 3 as in the fiducial model with the common values of a_{hg} and b_{hg} , but is five times more in mass M_{gh} as well as in the number of particles N_{hg} . We keep the single (hot or cold) gas particle mass the same at the initial time (in all our models).

As intended, the components except the gas halo in this model, and also in all other models of type DH, have (statistically) identical particle distributions at the initial time to those of the fiducial model DHi shown in Fig. 1. In all models of type DH, the initial profiles of the four components, such as the surface density profiles of both disks, the spherically averaged density profiles of the DM halo and the bulge, and the tangential velocity profiles of the four components, are also the same (or nearly the same for the properties of the DM halo) as those of the fiducial model presented in Fig. 2. But the gas halo of this model has higher density at each radius than that of the fiducial model DHi as shown in the second row-right column in Fig. 4 (see the black line for the initial density profile). The initial velocities of the halo gas particles in this model are set to zero as in the fiducial model. The temperature T with respect to the local gas density ρ_{local} for the gas particles in model DHi-f5 is presented in Fig. 3. As seen in the second row-leftmost column in the figure, the disk gas particles are initialized to have a single value of $T = 10000$ K (cyan dots) as in the fiducial model (and as also in all models with a gas disk), but the temperature of the halo gas particles is assigned in accordance with the hydrostatic equilibrium of the halo gas (magenta dots).

2.3.3. Model DHir

TABLE 2
PARAMETERS OF EACH COMPONENT OF THE INITIAL GALAXY MODELS

		Model DHi ^a /DHi-f5	Model DHn/DHn-f5	Model D	Model Hi
Star disk:					
disk model		exponential	exponential	exponential	exponential
a_{ds} [kpc] ^b	Length scale of star disk	3.5	3.5	3.5	3.5
z_{ds} [kpc]	Vertical disk scale height	0.35	0.35	0.35	0.35
b_{ds} [kpc]	Outer disk cut-off radius	42	42	42	42
M_{ds} [$10^{10} M_{\odot}$]	Total mass of star disk	4.4	4.4	4.4	5.0
N_{ds}	Number of particles	16384	16384	16384	16384
m_{ds} [$10^{10} M_{\odot}$]	Mass of individual particles	2.69×10^{-4}	2.69×10^{-4}	2.69×10^{-4}	3.05×10^{-4}
ϵ_{ds} [kpc]	Gravitational softening length	0.609/0.621	0.609/0.621	0.606	0.649
Gas disk:					
disk model		exponential	exponential	exponential	...
a_{dg} [kpc]	Length scale of gas disk	8.75	8.75	8.75	...
z_{dg} [kpc]	Vertical disk scale height	0.35	0.35	0.35	...
b_{dg} [kpc]	Outer disk cut-off radius	105	105	105	...
M_{dg} [$10^{10} M_{\odot}$]	Total mass of gas disk	0.6	0.6	0.6	...
N_{dg}	Number of particles	16384	16384	16384	...
m_{dg} [$10^{10} M_{\odot}$]	Mass of individual particles	3.66×10^{-5}	3.66×10^{-5}	3.66×10^{-5}	...
ϵ_{dg} [kpc]	Gravitational softening length	0.225/0.229	0.225/0.229	0.224	...
DM halo:					
halo model		NFW	NFW	NFW	NFW
a_{hd} [kpc]	Radial scale of DM halo	21	21	21	21
b_{hd} [kpc]	Radius to begin tapering	84	84	84	84
$M_{\text{hd}}(a_{\text{hd}})$ [$10^{10} M_{\odot}$]	Mass within radius a_{hd}	12.23/11.74	12.23/11.74	12.35	12.23
$M_{\text{hd}}(\infty) = M_{\text{hd}}$	Total mass of DM halo	118.8/114	118.8/114	120	118.8
N_{hd}	Number of particles	163840	163840	163840	163840
m_{hd} [$10^{10} M_{\odot}$]	Mass of individual particles	7.25×10^{-4} / 6.99×10^{-4}	7.25×10^{-4} / 6.99×10^{-4}	7.32×10^{-4}	7.25×10^{-4}
ϵ_{hd} [kpc]	Gravitational softening length	1	1	1	1
Gas halo:					
halo model		isothermal	NFW	...	isothermal
a_{hg} [kpc]	Radial scale, or radius of core	...	21
b_{hg} [kpc]	Radius to begin taper, or radius of taper	10.5	10.5
$M_{\text{hg}}(a_{\text{hg}})$ [$10^{10} M_{\odot}$]	Mass within radius a_{hg}	...	84
M_{hg} [$10^{10} M_{\odot}$]	Total mass of gas halo	420	420
N_{hg}	Number of particles	...	0.12/0.62
m_{hg} [$10^{10} M_{\odot}$]	Mass of individual particles	1.2/6.0	1.2/6.0	...	1.2
ϵ_{hg} [kpc]	Gravitational softening length	32768/163840	32768/163840	...	32768
		3.66×10^{-5}	3.66×10^{-5}	...	3.66×10^{-5}
		0.225/0.229	0.225/0.229	...	0.225
Bulge:					
bulge model		Hernquist	Hernquist	Hernquist	Hernquist
a_{b} [kpc]	Length scale of bulge	0.7	0.7	0.7	0.7
b_{b} [kpc]	Radius at which truncation starts	140	140	140	140
M_{b} [$10^{10} M_{\odot}$]	Total mass of bulge	1	1	1	1
N_{b}	Number of particles	8192	8192	8192	8192
m_{b} [$10^{10} M_{\odot}$]	Mass of individual particles	1.22×10^{-4}	1.22×10^{-4}	1.22×10^{-4}	1.22×10^{-4}
ϵ_{b} [kpc]	Gravitational softening length	0.410/0.419	0.410/0.419	0.408	0.410

^a Models DHi and DHir adopt the same parameter values.

^b Physical units are used in this table, h^{-1} kpc for the length and $10^{10} M_{\odot}$ for the mass parameter values. Conversion from dimensionless code units is described in the text.

Model DHir is designed to examine how the rotation of the gas halo makes a difference in the evolution. Thus the only difference between model DHir and the fiducial model DHi is whether the gas halo is spinning with non-zero initial velocities (in model DHir) or stationary at the beginning. Model DHir shares all parameter values of all components given in Table 2 with the fiducial model.

The initial distribution of the particles and some basic profiles are presented in Figs 1 and 2, which are common to both models DHir and DHi except the tangential velocity profile of the gas halo as designed (bottom-left panel of Fig. 2). The tangential velocities of the hot gas

in model DHir are assigned in such a way that the rotation curve of the gas halo has the same shape but has half the amplitude of that of the gas disk. The vertical velocity v_z is set to zero in this model. The choice of the gas halo rotation is not yet strongly restricted by current observations. For example, Moster et al. (2011) chose to set the spin of a gas halo in such a way that the specific angular momentum of the gas halo is four times that of the DM halo (see Sec. 2 of their paper for details). The test of different gas halo rotations would be the subject of future research.

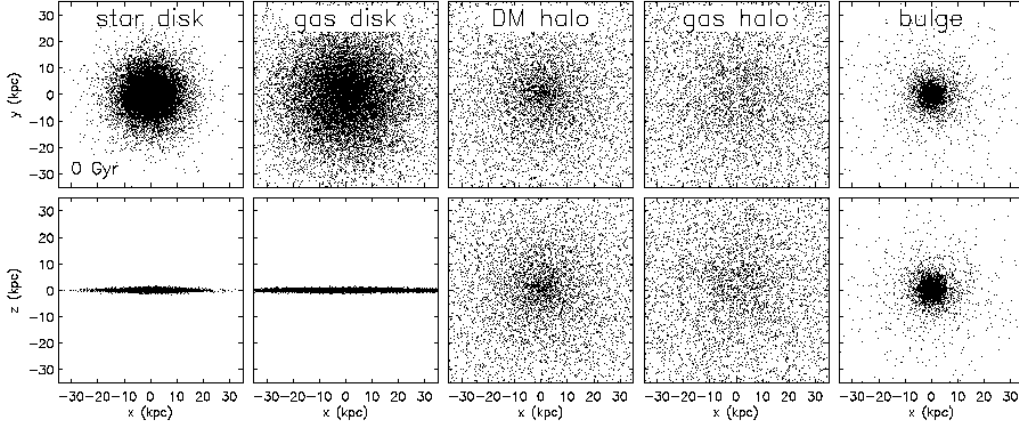


FIG. 1.— Initial particle distribution of models DHi and DHir. (Both models have exactly the same spatial distribution of the particles, but the latter has an additional spin of the gas halo.) The star or gas particles of the five components are displayed separately. The top and bottom rows show the distribution projected on to the x - y and x - z plane, respectively. For the DM halo component, every tenth particle is plotted; for the other components, every particle is plotted. Other initial galaxy models have a similar distribution as model DHi, except the gas halo (see text for the details).

2.3.4. Model DHn

As one of the DH type models, model DHn consists of the five components of both star and gas disks, both DM and gas halos, and a bulge. Differently from the fiducial model DHi, the gas halo of this model follows the NFW profile instead of the isothermal profile (Tables 1 and 2). The initial total mass of the gas halo is the same as that of the fiducial model. This model is used to examine how the different initial density profiles of the hot gas with equal mass make differences in the evolution.

The particle distributions in the four components except the gas halo in model DHn are identical to those of the fiducial model in Fig. 1. The gas halo follows the NFW profile like the DM halo but has five times fewer particles than in the DM halo. The spherically averaged density profile of the gas halo is presented in Fig. 4 (fourth row-right column). It is much higher within a few tens of kpc than that of the fiducial model and monotonically increasing towards the center. The initial tangential velocity of the gas halo is zero in this model. The temperature T of the gas particles at the initial time is presented in Fig. 3 with respect to the local density ρ_{local} (fourth row-leftmost panel).

2.3.5. Model DHn-f5

Model DHn-f5, like the previous model DHn, possesses a gas halo following the NFW profile but has five times more hot halo gas particles (Tables 1 and 2).

The spatial distribution of the hot gas following the NFW profile has the same shape as that of the DM halo shown in Fig. 1. The number of the hot halo gas particles is equal to that of the halo DM particles. A halo gas particle has 1/19 times lower mass than a DM particle. The spherically averaged density profile of the gas halo is specifically shown in Fig. 4 (fifth row-right column). Model DHn-f5 has the highest density at the inner part among all our models. The initial velocity of the gas halo is set to zero. The temperature of the gas as a function of the local gas density is plotted in Fig. 3 (fifth row-leftmost panel).

2.3.6. Model D

This model is composed of star and gas disks, a DM halo, and a bulge, but has no gas halo. The disk gas fraction and the total mass and the number of particles of each component are summarized in Tables 1 and 2.

The initial particle distributions of the four components in this model are equal to those of model DHi (Fig. 1). The initial T versus ρ_{local} plot for the gas disk is presented in Fig. 3 (bottom row-leftmost column; cyan dots only).

2.3.7. Model Hi

Model Hi is similar to the fiducial model DHi but has no gas disk. Its gas halo follows the isothermal density profile (Tables 1 and 2).

The initial particle distributions of the four components are equal to those of model DHi (Fig. 1). The spherically averaged initial density profile of the hot halo is shown in Fig. 4 (bottom row-right column; black line), which is the same as that of model DHi. The initial velocity of the gas halo is zero in this model. The surface density of the star disk (bottom row-left column in Fig. 4; black line) is highest among those of all models, as it has the more massive star disk without a gas disk. The initial T versus ρ_{local} diagram for the gas is presented in Fig. 3 (bottom row-leftmost column; magenta dots only); it is different from that of the fiducial model due to the different galactic potentials of the models.

3. SIMULATIONS

We use an early version of GADGET-3 code (originally described in Springel 2005) to evolve our galaxy models listed in Table 1 in isolation for 3 Gyr. The simulation code provides a model for galactic winds driven by star formation. We first run the seven models without including galactic winds. We then perform four more simulations using two of our models - models DHir and D - including winds with different sets of wind parameter values as summarized in Table 3. We will refer to the four runs with winds as ‘wind test runs’ (Table 3) and name them DHir-Wa, DHir-Wa-e1, DHir-Wi, and D-Wa.

In this section, we first describe the simulation code to

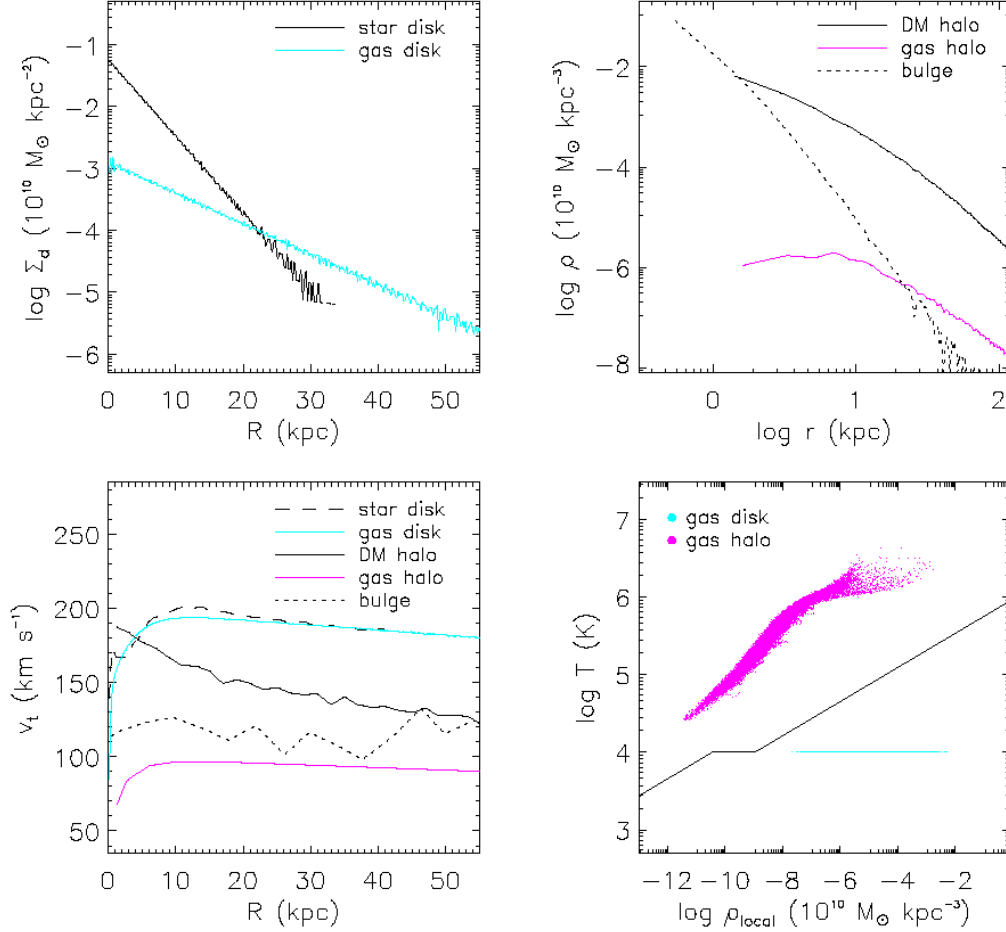


FIG. 2.— Initial properties of models DHi and DHir. *Top left*: Surface density profiles of the star and gas disk components. (Those of the other initial galaxy models are shown in Fig. 4.) *Top right*: Spherically averaged accumulated density profiles of the DM and gas halo and the bulge components. (The gas halo profiles of other models are also shown in Fig. 4.) *Bottom left*: Cylindrically averaged tangential velocity profiles of the star and gas disks, the DM and gas halos, and the bulge. The gas halo of model DHir only has the non-zero v_t (but zero in v_z) as drawn with the magenta solid. The gas halos of model DHi and all the other models have zero initial velocities in all three directions. (The v_t profiles of the four components except gas halo of the other models are similar as those shown in the panel.) *Bottom right*: Temperature against local density for the gas particles in the disk and halo components. The particles set as the gas disk and the gas halo are marked with cyan and magenta dots, respectively. The temperature of the disk gas particles is initialized to a single value of $T = 10000$ K. The temperature of the halo gas is determined to achieve hydrodynamic equilibrium. The disk and halo gas particles are initially well-separated by the black line in the panel. This line is chosen to use as a fixed criterion to divide the disk and halo gas at later times.

TABLE 3
WIND TEST RUNS

Name	Wind mode	Wind efficiency (η)
DHir-Wa	axial	2
DHir-Wa-e1	axial	1
DHir-Wi	isotropic	2
D-Wa	axial	2

explain some key processes. Then we present our simulation results.

3.1. The Simulation Code

The GADGET-3 code is a parallel TreeSPH code. The gravitational force is computed with a hierarchical multipole expansion and the hydrodynamical force with the smoothed particle hydrodynamics (SPH) technique in the entropy conservative formulation (Springel & Hern-

quist 2002). The code adopts radiative cooling and heating by photoionization (Katz et al. 1996). It also includes star formation and supernova feedback using the sub-resolution multiphase model of the interstellar medium (ISM) developed by Springel & Hernquist (2003). The ISM is pictured as a fluid comprised of condensed clouds in pressure equilibrium with an ambient hot medium. A thermal instability is assumed to be operating in the two-phase region exceeding a threshold density ρ_{th} . Star formation occurs in the dense regions, and converts cold clouds into stars on a time-scale constrained by observations (Kennicutt 1998). The mass fraction of massive stars among the newly formed stars is given by the parameter β . The massive stars are subject to die instantly as supernovae (with metal enrichment) releasing energy to the ambient phase. Some cold clouds are supposed to evaporate inside the supernova bubbles. The evaporation of cold clouds inside of supernova bubbles is handled by the simplified treatment of Springel & Hernquist (2003; see Sec. 3 of their paper for details). Only the density de-

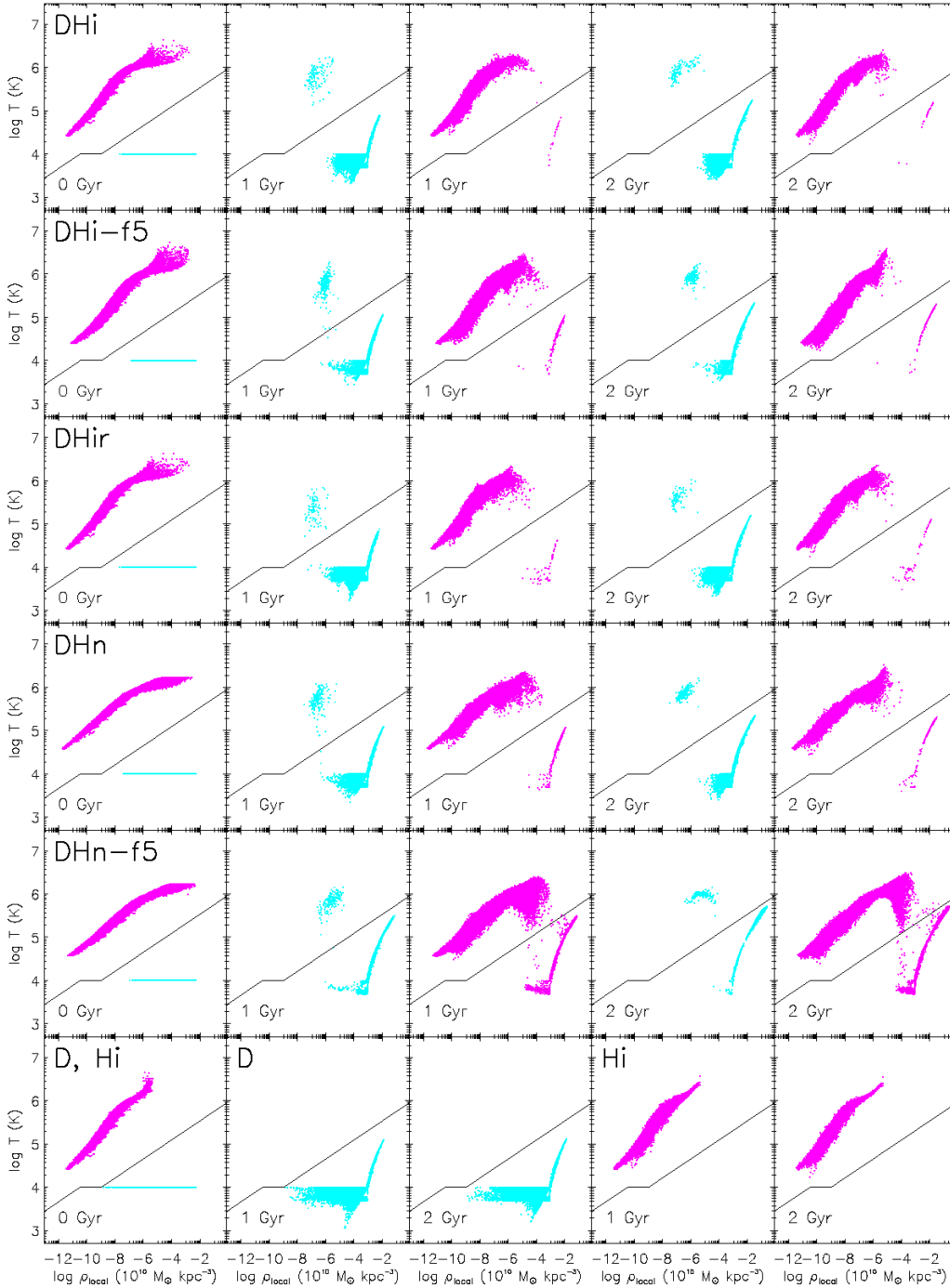


FIG. 3.— Temperature versus local density plots for the disk and halo gas of the galaxy models listed in Table 1. The top through fifth rows show the plots from each model of type DH. The first column presents those at the initial time, the second and third columns at $t = 1$ Gyr, and the fourth and fifth columns at $t = 2$ Gyr. The bottom row shows those from both models D and Hi. As same as the bottom-right panel of Fig. 2, the gas particles originally set as the disk and the halo are identified by cyan and magenta dots, respectively, and the same black line is imposed in each panel to divide the disk and halo gas at any time in all models. Those cyan dots appear above the black line are considered as halo gas at the time together with the magenta dots remain above the line. Similarly, those magenta dots lie below the line are counted as disk gas together with the cyans remain below the line.

pendency on the supernova evaporation is taken into account for simplicity (McKee & Ostriker 1977). The radiative cooling of the hot gas causes a corresponding increase of the cold gas. These processes - star formation, cloud evaporation and cloud growth - lead to a self-regulated cycle for star formation. The multiphase model is numerically implemented with the simplified treatment de-

scribed in Sec. 5.2 in Springel & Hernquist (2003) based on the fact that the conditions of the self-regulation are achieved quickly. In the treatment, the mass of each new star particle is set identically to $m_{\star} = m_0/N_g$, where m_0 is the initial gas mass before the star formation and N_g is number of star particles that may be generated in a gas particle at each star formation event.

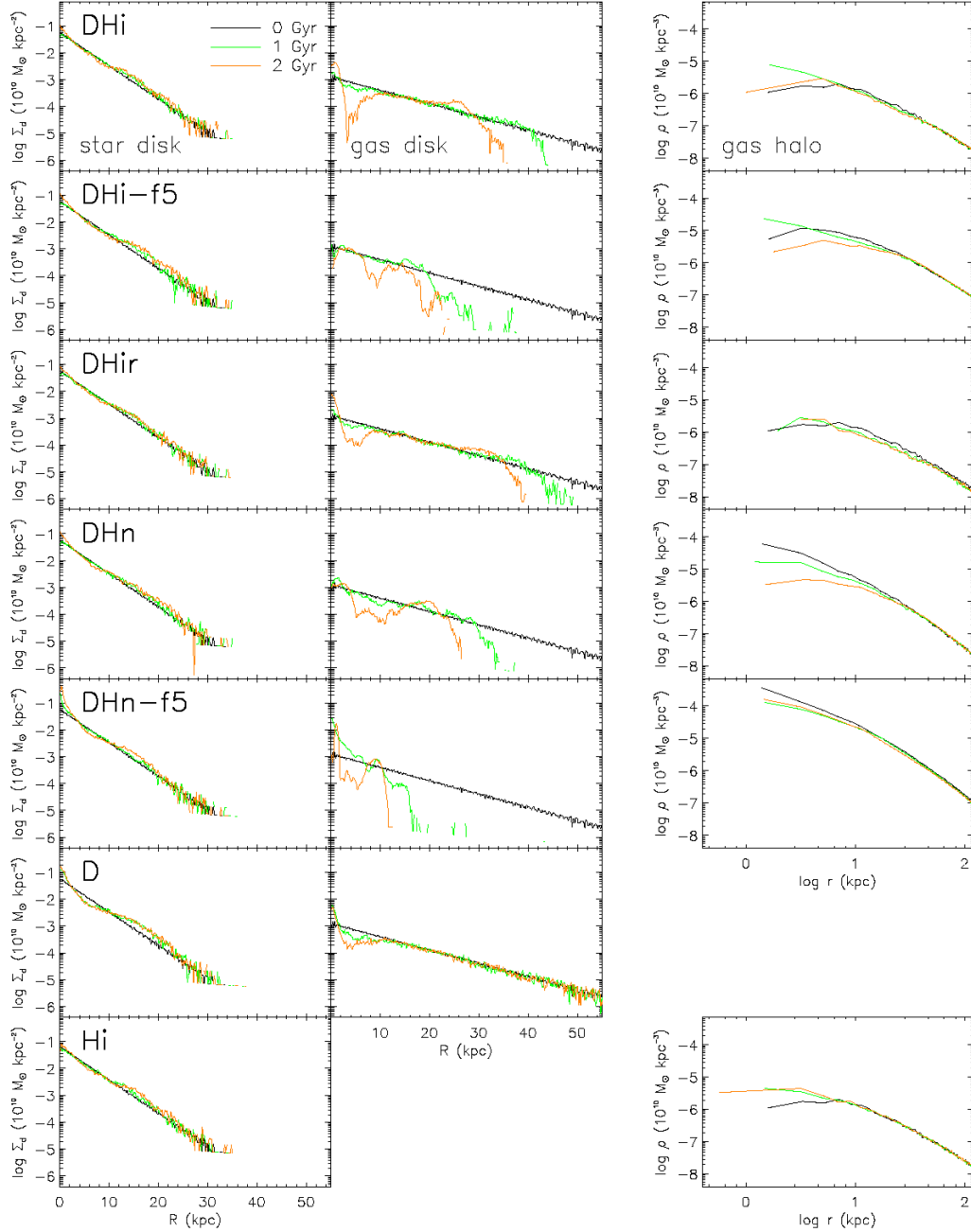


FIG. 4.— The surface and spherically averaged density profiles of the galaxy models at $t = 0, 1$, and 2 Gyr. The left and middle columns present the surface density profiles of the star and gas disks, respectively, and the right column the spherically averaged accumulated density profiles of the gas halos. Each row shows the profiles from each of the seven models.

The code also includes a model for galactic winds driven by star formation. The rate of the disk mass loss through a wind is assumed to be proportional to the star formation rate $\dot{M}_w = \eta \dot{M}_\star$, where η is a coefficient measuring the wind efficiency and \dot{M}_\star is the formation rate of long-lived stars. It is also assumed that the rate of energy loss through the wind is $\dot{M}_w v_w^2 / 2 = \chi \epsilon_{\text{SN}} \dot{M}_\star$, which is a fraction χ of the rate of energy generation by supernovae. Here v_w is the velocity of the wind, and $\epsilon_{\text{SN}} = u_{\text{SN}} \beta / (1 - \beta)$ represents the average return of the supernova energy from the stars formed following the Salpeter (1955) initial mass function. The velocity

of a particle is modified to $\vec{v}' = \vec{v} + v_w \hat{n}$ by the wind. The wind can be axial or isotropic (Springel & Hernquist 2003); the direction of the unit vector \hat{n} is chosen to be either random on the unit sphere in isotropic winds or as a random orientation along the direction of $\vec{v} \times \nabla \phi$ (ϕ is the gravitational potential) in axial winds.

In all of our simulations, the standard parameters for the multiphase model are used. They are mostly the same as those in Springel & Hernquist (2003), otherwise adjusted based on later observations or findings. The star formation time-scale t_0^* is set to 1.47 Gyr, and the mass fraction of massive star to $\beta = 0.1$. The ‘supernova temperature’ $T_{\text{SN}} = 2\mu u_{\text{SN}} / (3k)$ is chosen to be 10^8 K

which is equivalent to $\epsilon_{\text{SN}} = 4 \times 10^{48}$ erg/ M_{\odot} , the temperature of cold clouds T_c to 1000 K, and the parameter for supernova evaporation A_0 to 1000. We adopt $N_g = 2$, so a new star particle has a half the gas particle mass before the star formation event. Correspondingly, the total number of particles increases due to star formation even though the total mass of a system is kept constant.

In the wind test runs (Table 3), the effects of galactic winds driven by supernovae are included. Axial winds are tested in runs DHir-Wa, DHir-Wa-e1, and D-Wa, and isotropic winds in run DHir-Wi. The parameter of the wind efficiency is set to the standard value $\eta = 2$ in runs DHir-Wa, DHir-Wi, and D-Wa, while the half the value in DHir-Wa-e1 for comparison. The wind energy fraction parameter is set to the default value $\chi = 1$ in the runs with winds.

3.2. The Evolution of Galaxy Models Without Winds

Here we describe the evolution of our galaxy models without winds (listed in Table 1), focusing on the effects of the hot gas halo.

The distributions of particles in each simulation at four epochs are presented in Figs 5 through 11. We present the snapshots of the runs together with the evolution of the T - ρ_{local} plots (Fig. 3), the density profiles of the star disk, the gas disk, and the gas halo (Fig. 4), and the specific mass and the particle numbers of the components (Table 4). We begin with the runs of type DHi models.

3.2.1. Models having an isothermal gas halo

Here we describe the results for the galaxy models DHi (the fiducial model), DHi-f5, and DHir. These models contain a gas halo following the isothermal density profile (Eq. 3).

The snapshots of run DHi are presented in Fig. 5. The first two rows show the particle distribution of the star disk projected in the x - y and x - z planes, the third and fourth rows the gas disk, and the bottom two rows the gas halo, at $t = 0.1, 0.5, 1$, and 2 Gyr from the first to the fourth column sequentially.

In the first two rows in Fig. 5, the black dots represent the stars originally set as the star disk, and the blue and red dots indicate the stars added into the star disk from the gas originating from (i.e. initially set as) the gas disk and gas halo, respectively. In Table 4 we give the total mass and number of star disk particles (M_{ds} and N_{ds} , respectively) at each time; we also specify the number of star disk particles that are originally star disk particles ($N_{\text{ds,org}}$), produced from the disk gas ($N_{\text{ds,d2s}}$), and transformed from the halo gas ($N_{\text{ds,h2s}}$) separately. The total mass of the star disk as a whole is $M_{\text{ds}} = M_{\text{ds,org}} + M_{\text{ds,d2s}} + M_{\text{ds,h2s}}$. Similarly, the total number of the star disk particles is $N_{\text{ds}} = N_{\text{ds,org}} + N_{\text{ds,d2s}} + N_{\text{ds,h2s}}$. As time passes, spiral patterns and a central bar develop in the disk. Some deviation from the initial exponential surface density profiles are seen in Fig. 4 (first row-left column) due to those structures generated. The star disk grows in mass continuously (Table 4), as some gas turns into disk stars. The mass increases from the initial value $M_{\text{ds}} = 4.399 \times 10^{10} M_{\odot}$ to $4.524 \times 10^{10} M_{\odot}$ at $t = 2$ Gyr. The total number of star disk particles also increases from $N_{\text{ds}} = 16384$ at the beginning to 23182 at $t = 2$ Gyr.

The disk gas particles shown in the middle two rows in Fig. 5 are those determined as the disk gas by the criterion in the T - ρ_{local} plane (first row in Fig. 3). The black dots in the snapshots are the original disk gas particles still remaining in the disk (i.e. in the T - ρ_{local} plot, the gas particles among cyan dots lie below the criterion line). The magenta dots superimposed on the black dots are the originally hot halo particles that become the disk gas according to the T - ρ_{local} criterion (i.e. the gas particles among magenta lie below the criterion line). In the T - ρ_{local} diagrams at later times (second to fifth panels of the first row in Fig. 3), the disk gas particles, which are located below the black line, follow the finger-like pattern in the higher density region and show the sharp cut-off at $T \simeq 10000$ K in the lower density region. The negative correlation between T and ρ_{local} as shown by the finger-like feature results from the multiphase model (Springel & Hernquist 2003). The sharp cut-off appears because the minimum temperature a gas particle can reach through atomic radiative cooling processes is about 10000 K. As shown in the snapshots, some spiral patterns develop in the gas disk as in the star disk; warps are also generated as seen in the side view. The gas disk dissipates as time passes. Although some halo gas particles cool down to become the gas disk particles (mostly to the central part of the gas disk, as indicated with magenta dots), more gas particles turn into the disk stars. Some heated disk gas join the halo. The number of particles that are initially disk gas particles ($N_{\text{dg,org}}$) and that converted from the halo gas ($N_{\text{dg,h2d}}$) at each epoch are given in Table 4. As seen in the surface density profile of the gas disk (first row-middle column in Fig. 4), the size of the disk decreases by dissipation and the profile also evolves. The density at the innermost part of the disk increases at later times. The total mass of the gas disk $M_{\text{dg}} = M_{\text{dg,org}} + M_{\text{dg,h2d}}$ decreases from the initial value $M_{\text{dg}} = 0.6 \times 10^{10} M_{\odot}$ to $0.4726 \times 10^{10} M_{\odot}$ after 2 Gyr (Table 4).

The black dots in the bottom two rows in Fig. 5 are the gas particles that remain as the halo gas from the beginning (i.e. in the T - ρ_{local} diagram, the gas particles among magenta dots lie above the criterion line). The number of those particles is denoted by $N_{\text{hg,org}}$ in Table 4. The cyan circles superimposed on the black dots are those particles among originally set as the cold disk gas particles but having the properties of the gas halo according to the T - ρ_{local} criterion (i.e. the gas particle among cyan lie above the criterion line). The number of these transformed halo gas particles is $N_{\text{hg,d2h}}$ in Table 4. The cyan circles at early times are located mostly at the outer part of the gas disk. At later times, they appear more dispersed in both x - y and x - z views. The spherically averaged density profile of the gas halo is shown in Fig. 4 (first row-right column). At the initial time, the gas halo follows the isothermal density profile with the halo gas fraction $f_{\text{hg}} = 0.01$ (black line). It changes a bit (see olive and orange lines) from the initial profile mainly in the central part, as some halo gas are removed down to the disk (which subsequently turn into disk stars) and the gas particles are redistributed. The total mass of the gas halo $M_{\text{hg}} = M_{\text{hg,org}} + M_{\text{hg,d2h}}$ changes only a little from the initial value $1.2 \times 10^{10} M_{\odot}$ to $1.203 \times 10^{10} M_{\odot}$.

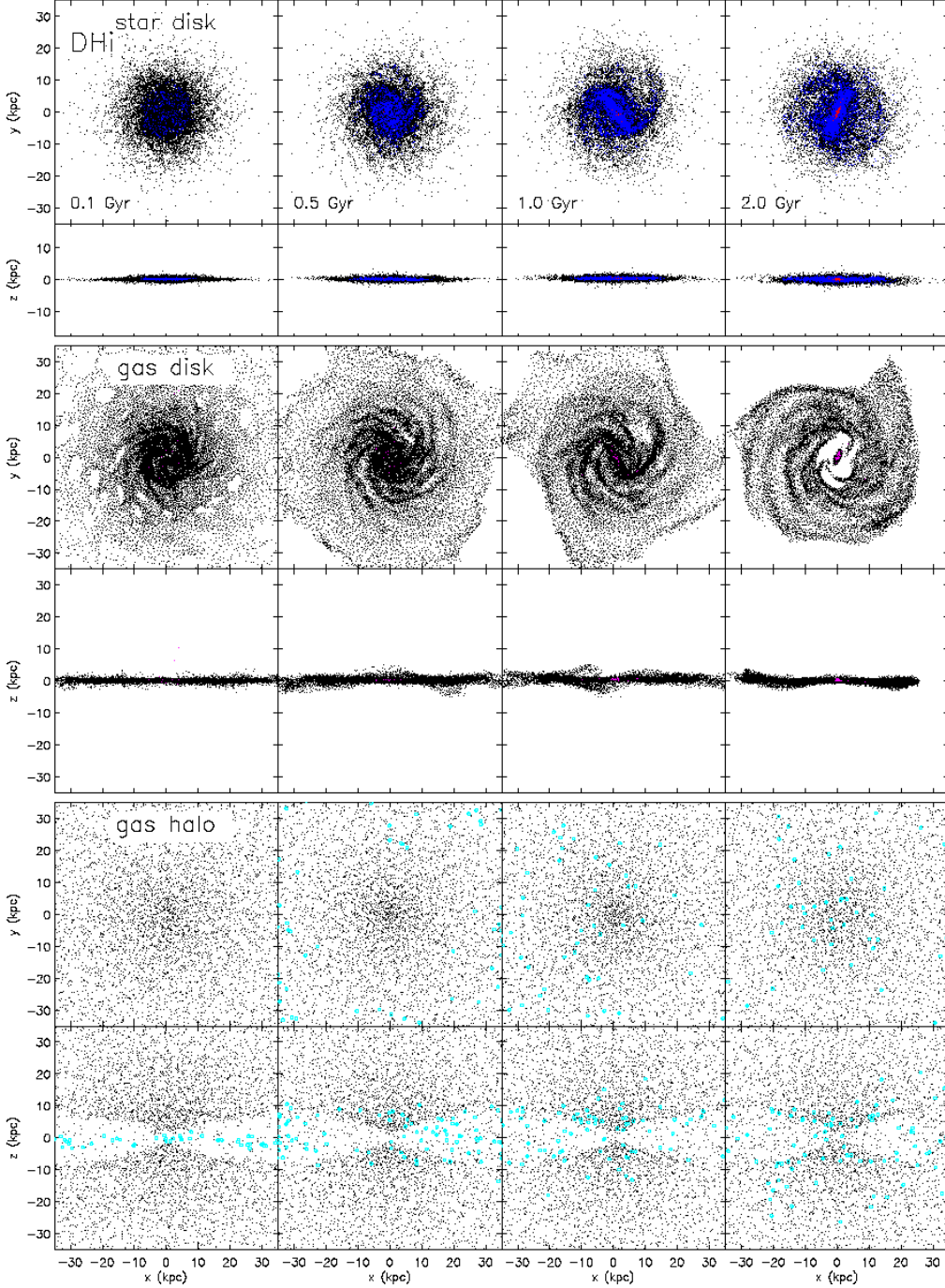


FIG. 5.— Four snapshots of the distribution of particles in run DHi. The first to fourth columns represent the system at $t = 0.1, 0.5, 1,$ and 2 Gyr, respectively. The first two rows show the distribution of the star particles in the disk seen in the x - y plane (first row) and the x - z plane (second row). The particles originally set as the star disk are marked with black dots and the particles turned into stars originating from the gas disk and the gas halo are indicated with blue and red dots, respectively. The third and fourth rows show the gas disk in the two projections. The particles originally set as the gas disk are marked in black dots and those accreted from the gas halo are in magenta dots. The bottom two rows show the particles in the gas halo. The particles originally set as the gas halo are marked in black dots and those included to the halo from originally the gas disk are in cyan circles. The cyan markers are bigger than the others to better distinguish the particles.

at $t = 2$ Gyr.

Fig. 6 shows the evolution of model DHi-f5. The model starts with five times more hot gas ($f_{\text{hg}} = 0.05$) than the fiducial model DHi. More blue and red dots are seen in the first two rows, compared to the previous run. Due to the massive gas halo, the gas disk particles (originat-

ing from the gas disk or the gas halo) are compressed, cooled, and turn into stars more quickly. Consequently, the surface density profile of the star disk (second row-left column in Fig. 4) deviates from the initial exponential profile more than that seen in run DHi. The star disk grows in mass from the initial value $M_{\text{ds}} = 4.399 \times$

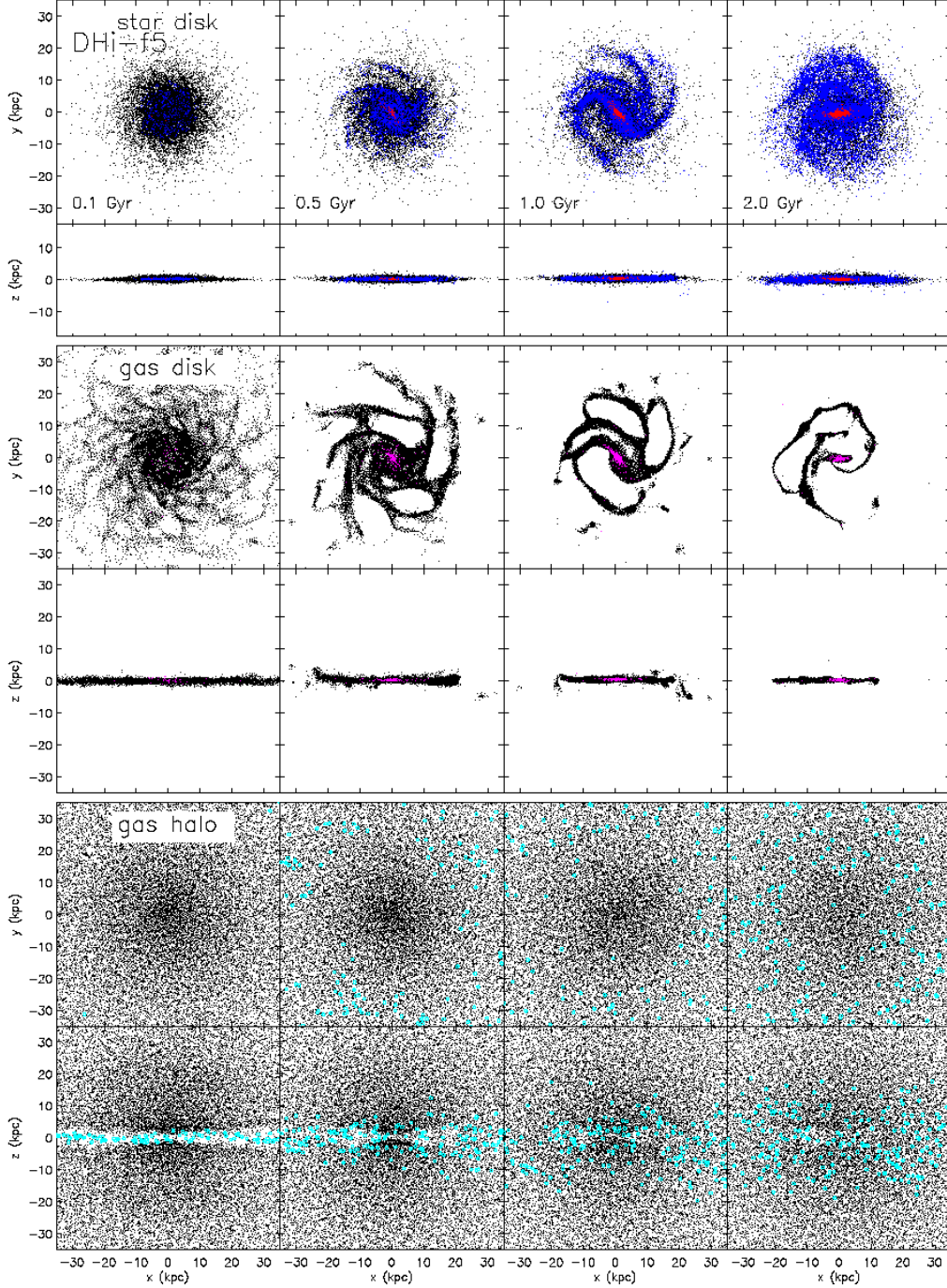


FIG. 6.— The same snapshots as Fig. 5, but from run DHI-f5.

$10^{10} M_{\odot}$ to $4.765 \times 10^{10} M_{\odot}$ at $t = 2$ Gyr (Table 4).

The gas disk and the gas halo particles of run DHI-f5 plotted in Fig. 6 are those determined in accordance with the $T\text{-}\rho_{\text{local}}$ criterion. The gas disk dissipates very quickly as clearly seen in the third and fourth rows in Fig. 6 and also in the surface density profile (second row-middle column in Fig. 4). The gas disk diminishes in mass by star formation from the initial value $M_{\text{ds}} = 0.6 \times 10^{10} M_{\odot}$ to $0.2411 \times 10^{10} M_{\odot}$ at $t = 2$ Gyr (Table 4). The gas halo changes mostly within a few tens of kpc as seen in both the snapshots (Fig. 6) and the density

profile (Fig. 4). The change is contributed by the halo gas particles in the central part which cool down to the disk (magenta dots in the snapshots) as well as the gas particles originating from the gas disk which are heated by the hot gas and moved to the more diffuse gas halo (cyan circles in the snapshots). Overall, the gas halo changes in mass slightly from the initial value of $M_{\text{ds}} = 5.998 \times 10^{10} M_{\odot}$ to $5.991 \times 10^{10} M_{\odot}$ at $t = 2$ Gyr (Table 4).

Four snapshots of run DHir are shown in Fig. 7. The model has a rotating gas halo following the isothermal

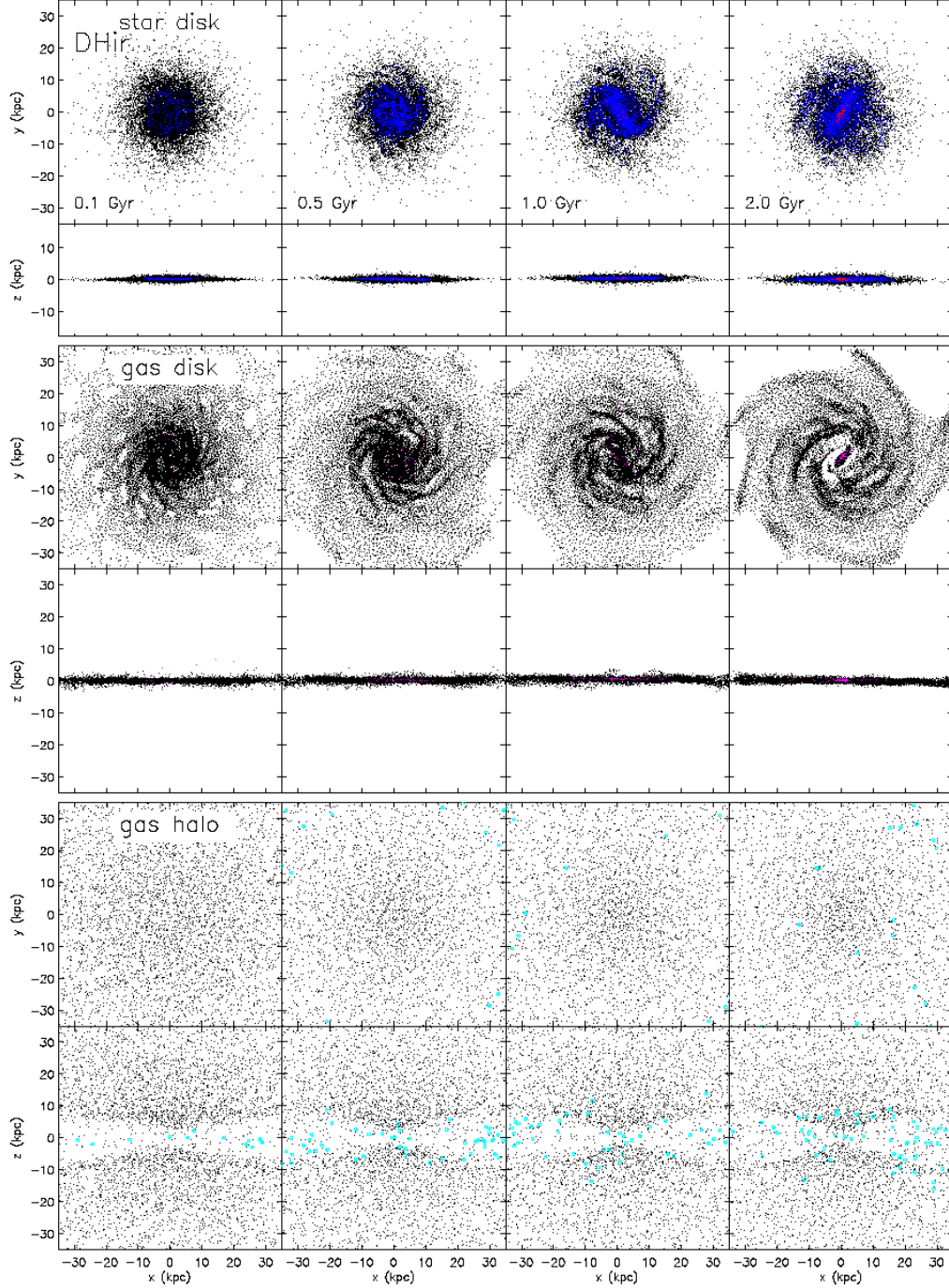


FIG. 7.— The same snapshots as Fig. 5, but from run DHir.

density profile with $f_{\text{hg}} = 0.01$. Compared to the first run DHi, fewer number of gas particles originating from the gas disk turn into stars (blue dots in the snapshots; also refer to $N_{\text{ds,d2s}}$ in Table 4). On the other hand, more gas particles originating from the hot halo cool down to the gas disk (magenta dots; $N_{\text{dg,h2d}}$). The accreted gas particles mostly appear in the inner part of the disk but rarely in the outer part. The rotation of the hot halo contributes the gas halo particles to settle down to the disk a bit more efficiently, but it also make the cooling time of the compressed gas particles in the disk longer. This re-

sults in less massive star disk (M_{ds}) and more massive gas disk (M_{dg}) than those of run DHi (and also than all the runs of types DH and D without winds) as shown in Table 4. The gas disk in this run thus dissipates more slowly than the two previous runs as seen in both the snapshots and its surface density profile (Fig. 4). Fewer number of gas particles originating from the disk are heated and included into the halo (cyan circles; $N_{\text{hg,d2h}}$). The gas halo keeps its initial mass (M_{hg}) for at least a couple of Gyr (Table 4).

3.2.2. Models having an NFW-profile gas halo

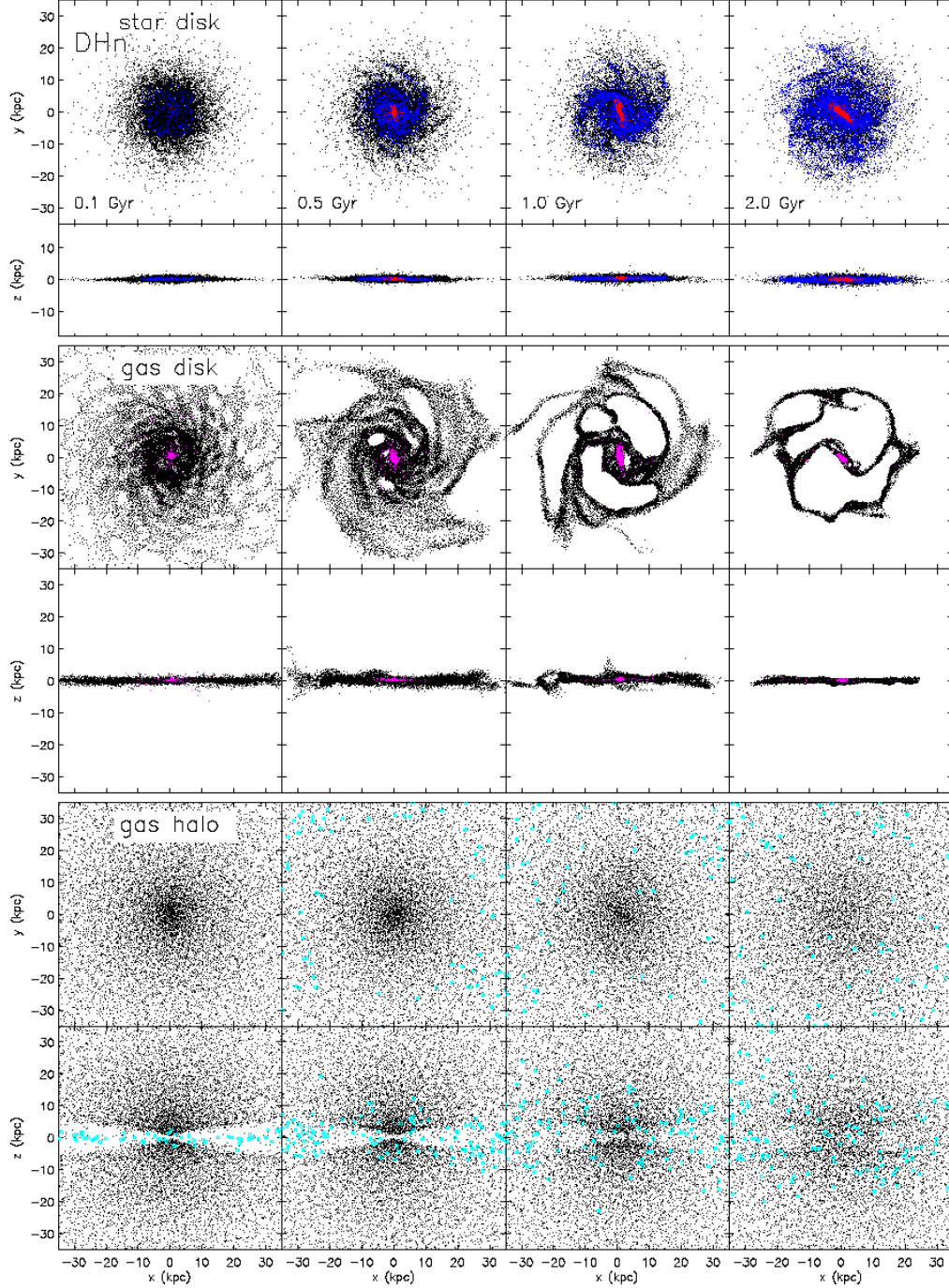


FIG. 8.— The same snapshots as Fig. 5, but from run DHn.

Models DHn and DHn-f5 have a gas halo following the NFW density profile (Eq. 2) with $f_{\text{hg}} = 0.01$ and 0.05 , respectively.

Fig. 8 shows the four snapshots from a run of DHn. Compared to the run with the fiducial model DHi, more stars are added into the disk from the disk and the halo gas (blue and red dots; see also Table 4). This is led by the higher density of the inner part of the gas halo in model DHn, as seen in the spherically averaged density profiles (Fig. 4), although the initial halo gas fraction and thus the initial total mass of the hot gas are iden-

tical in both models. Compared to the run of DHi-f5 having a heavier gas halo, fewer disk gas particles turn into the stars (blue dots; except at $t = 0.1$ Gyr as shown in Table 4). This is in part because the less massive gas halo in run DHn exerts overall weaker compression to the gas disk. Note that, however, more halo gas particles become the disk gas (magenta dots) in run DHn compared to run DHi-f5 and subsequently turns into stars (red dots), due to the higher central density of the gas halo (Fig. 4), even though the initial total mass of the gas halo is five times less than that of model DHi-f5. In

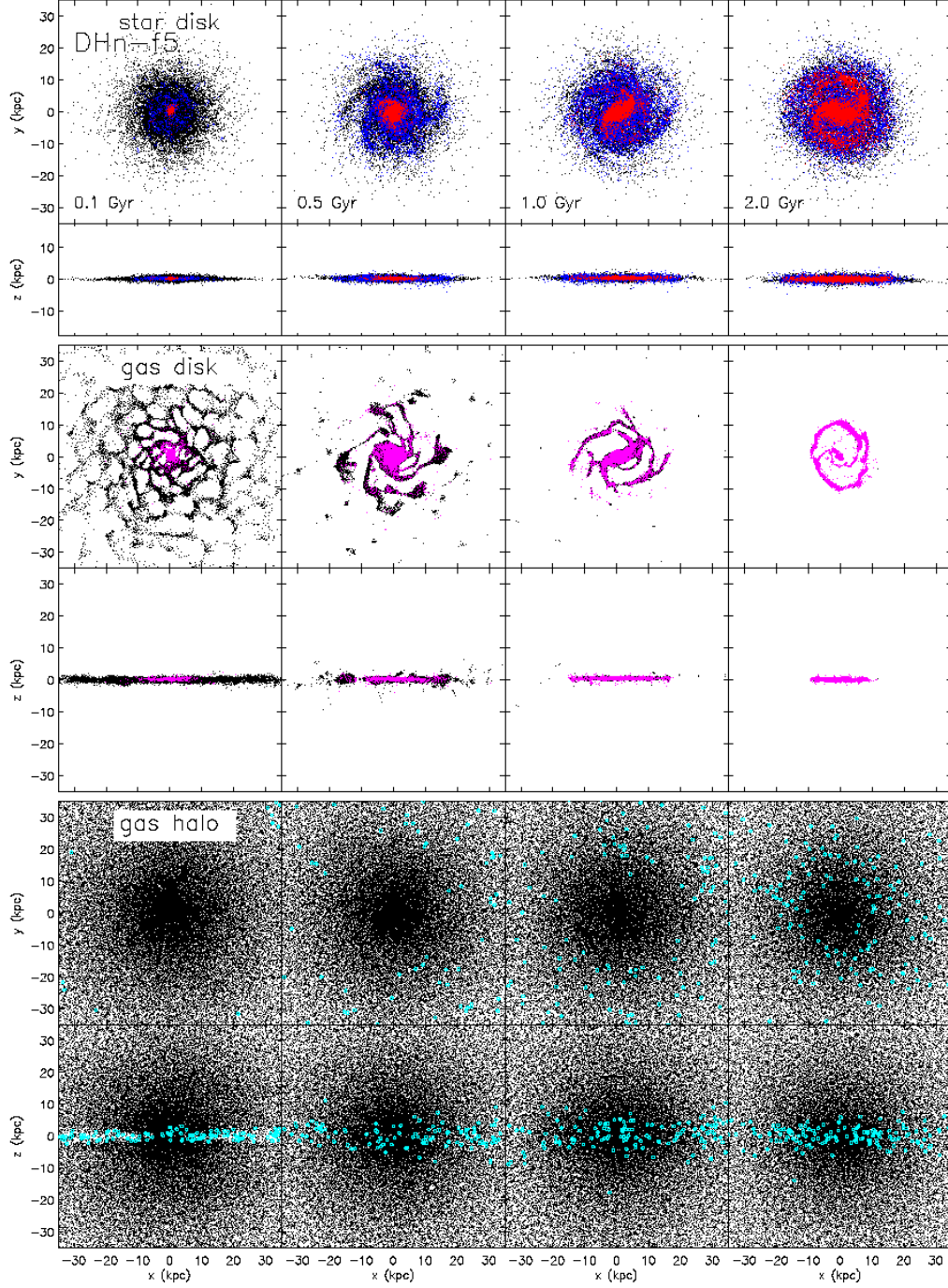


FIG. 9.— The same snapshots as Fig. 5, but from run DHn-f5.

this run DHn, the total mass of the star disk increases from $M_{\text{ds}} = 4.399 \times 10^{10} M_{\odot}$ at the initial time to $4.657 \times 10^{10} M_{\odot}$ at $t = 2$ Gyr (Table 4). The gas disk and the gas halo decrease in mass from $M_{\text{dg}} = 0.6 \times 10^{10} M_{\odot}$ at $t = 0$ to $0.3646 \times 10^{10} M_{\odot}$ after 2 Gyr, and from $M_{\text{hg}} = 1.2 \times 10^{10} M_{\odot}$ at $t = 0$ to $1.177 \times 10^{10} M_{\odot}$ after 2 Gyr, respectively.

Fig. 9 shows the the four snapshots from the simulation of model DHn-f5. Its gas halo has the highest central density among all our models (Fig. 4). Star formation in the disk (blue and red dots in Fig. 9) occurs most actively

in this model run, ending up with the most massive star disk of $M_{\text{ds}} = 5.474 \times 10^{10} M_{\odot}$ at $t = 2$ Gyr which is 124% of its initial mass (Table 4). The surface density of the star disk in the central part becomes higher than all the other runs (Fig. 4). The gas disk also dissipates very quickly in this run. Most of the original disk gas has been consumed by $t = 2$ Gyr (black dots in the middle two rows in Fig. 9; $N_{\text{dg,org}}$ in Table 4); the gas particles seen in the disk at later times are mostly those accreted from the hot halo (magenta dots; $N_{\text{dg,h2d}}$). The total mass of the gas disk decreases to $M_{\text{dg}} = 0.2252 \times 10^{10} M_{\odot}$ at

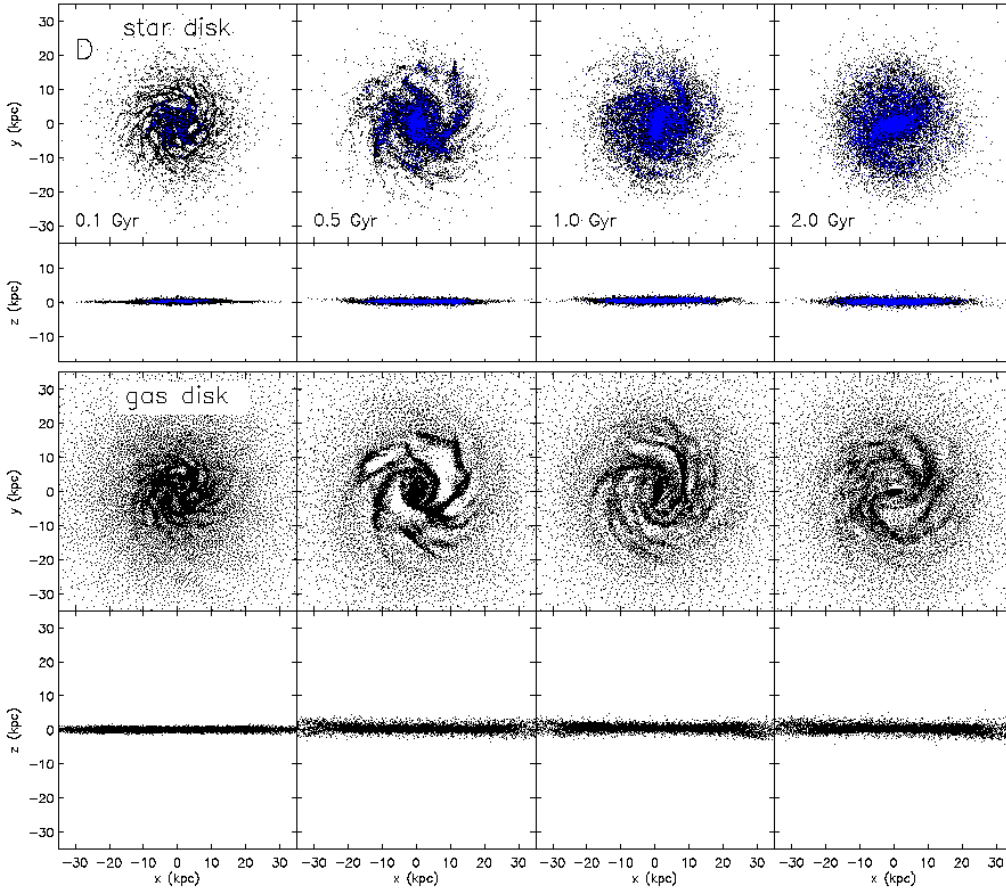


FIG. 10.— The same snapshots as Fig. 5, but from run D. The initial galaxy model D does not have a gas halo.

$t = 2$ Gyr, which is 38% of its initial mass (Table 4). The total mass of the gas halo also decreases to $5.298 \times 10^{10} M_{\odot}$ at $t = 2$ Gyr, 88% of the initial mass.

3.2.3. Models D and Hi

The four snapshots from run D is presented in Fig. 10. The galaxy model D does not have a gas halo at the set-up. New stars are added into the disk as some gas in the disk turn into stars (blue dots). None of the gas particles initially set as the disk gas become the halo gas according to the T - ρ_{local} criterion throughout the simulation (left three panels of the bottom row in Fig. 3). The star disk grows in mass from the initial value of $M_{\text{ds}} = 4.399 \times 10^{10} M_{\odot}$ to $4.518 \times 10^{10} M_{\odot}$ at $t = 2$ Gyr (Table 4). The gas disk mass M_{dg} decreases by the same amount through star formation. The radial extent of the gas disk is maintained well compared to all runs of type DH models which possess a gas halo, as seen in the snapshots (Fig. 10) and in the surface density profile (Fig. 4).

Fig. 11 shows the snapshots from run Hi. This model is initialized with the gas halo component following the isothermal density profile with the halo gas fraction $f_{\text{hg}} = 0.01$ but does not have a gas disk. Over the course of the simulation, no gas particles initially set as the hot halo gas cool down to the disk according to the T - ρ_{local} criterion (leftmost panel and two rightmost panels in the bottom row in Fig. 3). Consequently, no new stars are formed in the star disk; the masses of the star disk and the gas halo remain unchanged from the initial values

(Table 4). The surface density profile of the star disk deviates from the initial exponential profile due to the central bar and the spiral patterns developed in the star disk, as seen in Fig. 4. It is also seen that the spherically averaged density profile of the gas halo increases in the central part.

3.3. The Evolution of Galaxy Models With Winds

The evolution of the four wind test runs listed in Table 3 are discussed here. As noted earlier, galactic winds driven by supernova are included in these runs.

The temperature T of the gas components in the models with respect to the local density ρ_{local} are shown in Fig. 12, and the evolution of the density profiles of the star and gas disks and the gas halo in Fig. 13. The particle distributions of the three components in each run at four epochs are presented in Figs 14–17. The total mass and number of particles of the components are given in Table 4.

3.3.1. Runs DHir-Wa, DHir-Wa-e1, and DHir-Wi

The galaxy model DHir is used for these three runs. The initial model contains a gas halo with the isothermal density profile and the halo gas fraction of $f_{\text{hg}} = 0.01$ as in the fiducial model DHi but has an additional rotation for the gas halo. The three runs are thus identical to one another at the start of the runs, and also to run DHir without winds in Sec. 3.2.1. However, they are subject to different evolution due to the different wind parameters.

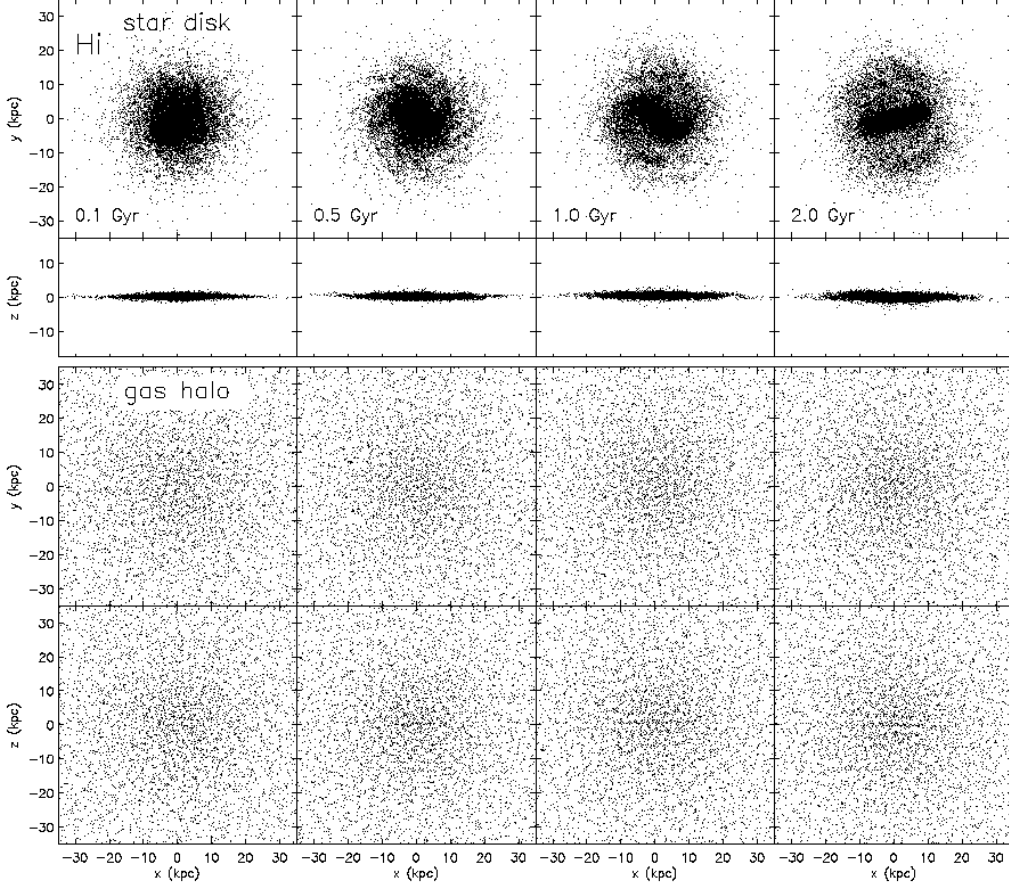


FIG. 11.— The same snapshots as Fig. 5, but from run Hi. The initial galaxy model Hi does not have a gas disk.

The snapshots of run DHir-Wa at $t = 0.1, 0.5, 1$, and 2 Gyr are presented in Fig. 14. This run accounts for supernova-driven galactic winds in axial mode with the wind efficiency of 2 as summarized in Table 3. Compared to run DHir without winds, new stars are formed less actively in the star disk from the gas disk and the gas halo particles (blue and red dots in the first two rows), as some gas are blown away by the winds. Fig. 13 shows that the surface density of the disk at the center does not rise as high as that of run DHir at later times. The total mass of the star disk grows more slowly than in run DHir, and becomes $M_{\text{ds}} = 4.449 \times 10^{10} M_{\odot}$ at $t = 2$ Gyr which is only a 1% increase from the initial mass (Table 4). However, the mass of the gas disk is reduced more than in run DHir. This is because, although fewer gas particles in the disk turn into stars, more gas is expelled from the disk by the energetic winds (as seen cyan circles in the bottom two rows) and also fewer gas particles from the halo settle down onto the disk (magenta dots in the middle two rows). The phenomena can be seen in the T - ρ_{local} diagrams (Fig. 12) as well. In the first row of Fig. 12, more gas particles originating from the disk (cyan dots) appear above the criterion line at both $t = 1$ and 2 Gyr (first and third panels; see also $N_{\text{hg,d2h}}$ in Table 4) compared to those of run DHir, and less gas originating from the halo (magenta dots) lie below the black line (second and forth panels; $N_{\text{dg,h2d}}$ in Table 4). The surface density of the gas disk and the spherically averaged density of the gas halo (Fig. 13) show less density in the cen-

tral region at later times than those of run DHir, due to the gas removal from the center by the winds. The total mass of the gas halo increases through the gas ejected from the disk while less amount of gas is lost to the disk; it becomes $M_{\text{hg}} = 1.305 \times 10^{10} M_{\odot}$ at $t = 2$ Gyr, which is a 9% increase from the initial mass, while that of the run DHir is almost unchanged for a few Gyr.

Four snapshots of run DHir-Wa-e1 are presented in Fig. 15. In this simulation, the axial mode of stellar winds is chosen as in the previous run DHir-Wa, but with half the strength of the wind efficiency $\eta = 1$ for comparison. Mostly, star formation occurs more actively in this run than in run DHir-Wa; the total star disk mass increases to $M_{\text{ds}} = 4.469 \times 10^{10} M_{\odot}$ at $t = 2$ Gyr, which is a bit greater than that of run DHir-Wa. The total mass of the gas disk decreases less slowly than that in run DHir-Wa, because fewer disk gas are expelled from the disk by the weaker winds (cyan circles in the snapshots; refer to $N_{\text{hg,d2h}}$ in Table 4; see also the T - ρ_{local} plots in Fig. 12), although more disk gas turns into stars than in run DHir-Wa (blue dots; $N_{\text{ds,d2s}}$). The total mass of the gas halo increases to $M_{\text{hg}} = 1.271 \times 10^{10} M_{\odot}$ at $t = 2$ Gyr, which is smaller than that of run DHir-Wa. The surface density of the gas disk (Fig. 13) rises at the center at later times than in run DHir-Wa. The spherically averaged density of the gas halo changes mainly in the inner part.

Four snapshots of run DHir-Wi are presented in Fig. 16. This run adopts the isotropic mode for stel-

TABLE 4
MASS AND NUMBER OF PARTICLES OF THE STAR AND GAS DISKS, AND THE GAS HALO IN ALL OF OUR SIMULATIONS.

	$N_{\text{ds}} (M_{\text{ds}})^{\text{a}}$	$N_{\text{ds,org}}$	$N_{\text{ds,d2s}}$	$N_{\text{ds,h2s}}$	$N_{\text{dg}} (M_{\text{dg}})$	$N_{\text{dg,org}}$	$N_{\text{dg,h2d}}$	$N_{\text{hg}} (M_{\text{hg}})$	$N_{\text{hg,org}}$	$N_{\text{hg,d2h}}$
DHi										
$t = 0$ Gyr	16384 (4.399)	16384	0	0	16384 (0.6000)	16384	0	32768 (1.200)	32768	0
$t = 0.1$ Gyr	16780 (4.407)	16384	396	0	16270 (0.5888)	16260	10	32877 (1.204)	32758	119
$t = 0.5$ Gyr	18165 (4.432)	16384	1780	1	16127 (0.5629)	16115	12	32890 (1.204)	32756	134
$t = 1$ Gyr	19678 (4.460)	16384	3286	8	15794 (0.5359)	15771	23	32871 (1.203)	32745	126
$t = 2$ Gyr	23182 (4.524)	16384	6756	42	14089 (0.4726)	14057	32	32849 (1.203)	32724	125
DHi-f5										
$t = 0$ Gyr	16384 (4.399)	16384	0	0	16384 (0.6000)	16384	0	163840 (5.998)	163840	0
$t = 0.1$ Gyr	16851 (4.408)	16384	465	2	16190 (0.5848)	16149	41	164022 (6.004)	163799	223
$t = 0.5$ Gyr	19244 (4.452)	16384	2813	47	16074 (0.5450)	15904	170	163912 (6.000)	163668	244
$t = 1$ Gyr	24232 (4.543)	16384	7624	224	15200 (0.4598)	14911	289	163745 (5.994)	163505	240
$t = 2$ Gyr	36350 (4.765)	16384	19290	676	9795 (0.2411)	9648	147	163658 (5.991)	163416	242
DHir										
$t = 0$ Gyr	16384 (4.399)	16384	0	0	16384 (0.6000)	16384	0	32768 (1.200)	32768	0
$t = 0.1$ Gyr	16724 (4.405)	16384	340	0	16363 (0.5932)	16344	19	32784 (1.200)	32749	35
$t = 0.5$ Gyr	18079 (4.430)	16384	1689	6	16212 (0.5670)	16172	40	32823 (1.202)	32728	95
$t = 1$ Gyr	19532 (4.457)	16384	3134	14	15903 (0.5410)	15850	53	32805 (1.201)	32713	92
$t = 2$ Gyr	22621 (4.513)	16384	6173	64	14452 (0.4856)	14389	63	32775 (1.200)	32687	88
DHn										
$t = 0$ Gyr	16384 (4.399)	16384	0	0	16384 (0.6000)	16384	0	32768 (1.200)	32768	0
$t = 0.1$ Gyr	16860 (4.408)	16384	473	3	16378 (0.5915)	16218	160	32763 (1.199)	32608	155
$t = 0.5$ Gyr	18752 (4.443)	16384	2173	195	16438 (0.5665)	16015	423	32499 (1.190)	32318	181
$t = 1$ Gyr	21935 (4.501)	16384	4977	574	15862 (0.5164)	15318	544	32276 (1.182)	32087	189
$t = 2$ Gyr	30479 (4.657)	16384	12743	1352	12060 (0.3646)	11832	228	32148 (1.177)	31955	193
DHn-f5										
$t = 0$ Gyr	16384 (4.399)	16384	0	0	16384 (0.6000)	16384	0	163840 (5.998)	163840	0
$t = 0.1$ Gyr	17419 (4.418)	16384	849	186	17443 (0.6214)	16077	1366	162739 (5.957)	162462	277
$t = 0.5$ Gyr	27734 (4.607)	16384	7821	3529	19764 (0.5906)	14926	4838	158422 (5.799)	158242	180
$t = 1$ Gyr	43271 (4.892)	16384	16762	10125	17101 (0.4384)	11364	5737	154810 (5.667)	154646	164
$t = 2$ Gyr	75100 (5.474)	16384	31139	27577	8256 (0.2252)	1213	7043	144716 (5.298)	144570	146
D										
$t = 0$ Gyr	16384 (4.399)	16384	0	...	16384 (0.6000)	16384	...	0 (0.0)	...	0
$t = 0.1$ Gyr	16761 (4.406)	16384	377	...	16376 (0.5931)	16376	...	0 (0.0)	...	0
$t = 0.5$ Gyr	18839 (4.444)	16384	2455	...	16150 (0.5551)	16150	...	0 (0.0)	...	0
$t = 1$ Gyr	20767 (4.480)	16384	4383	...	15507 (0.5198)	15507	...	0 (0.0)	...	0
$t = 2$ Gyr	22860 (4.518)	16384	6476	...	14342 (0.4815)	14342	...	0 (0.0)	...	0
Hi										
$t = 0$ Gyr	16384 (5.000)	16384	...	0	0 (0.0)	...	0	32768 (1.200)	32768	...
$t = 0.1$ Gyr	16384 (5.000)	16384	...	0	0 (0.0)	...	0	32768 (1.200)	32768	...
$t = 0.5$ Gyr	16384 (5.000)	16384	...	0	0 (0.0)	...	0	32768 (1.200)	32768	...
$t = 1$ Gyr	16384 (5.000)	16384	...	0	0 (0.0)	...	0	32768 (1.200)	32768	...
$t = 2$ Gyr	16384 (5.000)	16384	...	0	0 (0.0)	...	0	32768 (1.200)	32768	...
DHir-Wa										
$t = 0$ Gyr	16384 (4.399)	16384	0	0	16384 (0.6000)	16384	0	32768 (1.200)	32768	0
$t = 0.1$ Gyr	16720 (4.405)	16384	336	0	16054 (0.5823)	16040	14	33089 (1.211)	32754	335
$t = 0.5$ Gyr	17521 (4.420)	16384	1137	0	15022 (0.5338)	15004	18	34071 (1.245)	32750	1321
$t = 1$ Gyr	18137 (4.431)	16384	1753	0	14184 (0.4985)	14162	22	34817 (1.269)	32746	2071
$t = 2$ Gyr	19124 (4.449)	16384	2737	3	12594 (0.4441)	12575	19	36102 (1.305)	32749	3353
DHir-Wa-e1										
$t = 0$ Gyr	16384 (4.399)	16384	0	0	16384 (0.6000)	16384	0	32768 (1.200)	32768	0
$t = 0.1$ Gyr	16699 (4.405)	16384	315	0	16195 (0.5877)	16179	16	32951 (1.206)	32752	199
$t = 0.5$ Gyr	17783 (4.425)	16384	1398	1	15505 (0.5469)	15484	21	33564 (1.227)	32747	817
$t = 1$ Gyr	18642 (4.441)	16384	2256	2	14830 (0.5150)	14806	24	34080 (1.243)	32744	1336
$t = 2$ Gyr	20218 (4.469)	16384	3828	6	13168 (0.4580)	13145	23	35134 (1.271)	32743	2391
DHir-Wi										
$t = 0$ Gyr	16384 (4.399)	16384	0	0	16384 (0.6000)	16384	0	32768 (1.200)	32768	0
$t = 0.1$ Gyr	16752 (4.406)	16384	368	0	16117 (0.5840)	16110	7	33026 (1.209)	32761	265
$t = 0.5$ Gyr	17609 (4.422)	16384	1224	1	14993 (0.5314)	14985	8	34095 (1.246)	32760	1335
$t = 1$ Gyr	18268 (4.434)	16384	1883	1	14164 (0.4958)	14156	8	34822 (1.269)	32760	2062
$t = 2$ Gyr	19434 (4.455)	16384	3047	3	12495 (0.4369)	12489	6	36151 (1.307)	32761	3390
D-Wa										
$t = 0$ Gyr	16384 (4.399)	16384	0	...	16384 (0.6000)	16384	...	0 (0.0)	...	0
$t = 0.1$ Gyr	16716 (4.405)	16384	332	...	16355 (0.5932)	16355	...	21 (0.0007507)	...	21
$t = 0.5$ Gyr	18193 (4.432)	16384	1809	...	15395 (0.5387)	15395	...	849 (0.02823)	...	849
$t = 1$ Gyr	18947 (4.446)	16384	2563	...	14435 (0.5019)	14435	...	1629 (0.05125)	...	1629
$t = 2$ Gyr	19417 (4.455)	16384	3033	...	13808 (0.4824)	13808	...	2071 (0.06211)	...	2071

^a All masses in this table are in units of $10^{10} M_{\odot}$.

lar winds. The wind efficiency is chosen to $\eta = 2$ as in run DHir-Wa. The number of newly formed stars in the disk is generally similar as that of run DHir-Wa. The total masses of the star and the gas disks at 2 Gyr are also close to those of run DHir-Wa. In the snapshots, the expelled gas from the disk by the winds shows weaker bipolar pattern (cyan circles; also refer to the T - ρ_{local} plots in Fig. 12) than in run DHir-Wa, due to the different wind modes used in the two simulations. The evolution

of surface density profile of the gas disk and the spherically averaged density profile of the gas halo (Fig. 13) are not identical to those of run DHir-Wa, however, the amount of the ejected gas as well as the mass of each component are close to those of run DHir-Wa (Table 4).

3.3.2. Run D-Wa

This run uses the galaxy model D, which does not have a gas halo. To compare with run D in Sec. 3.2.3 without

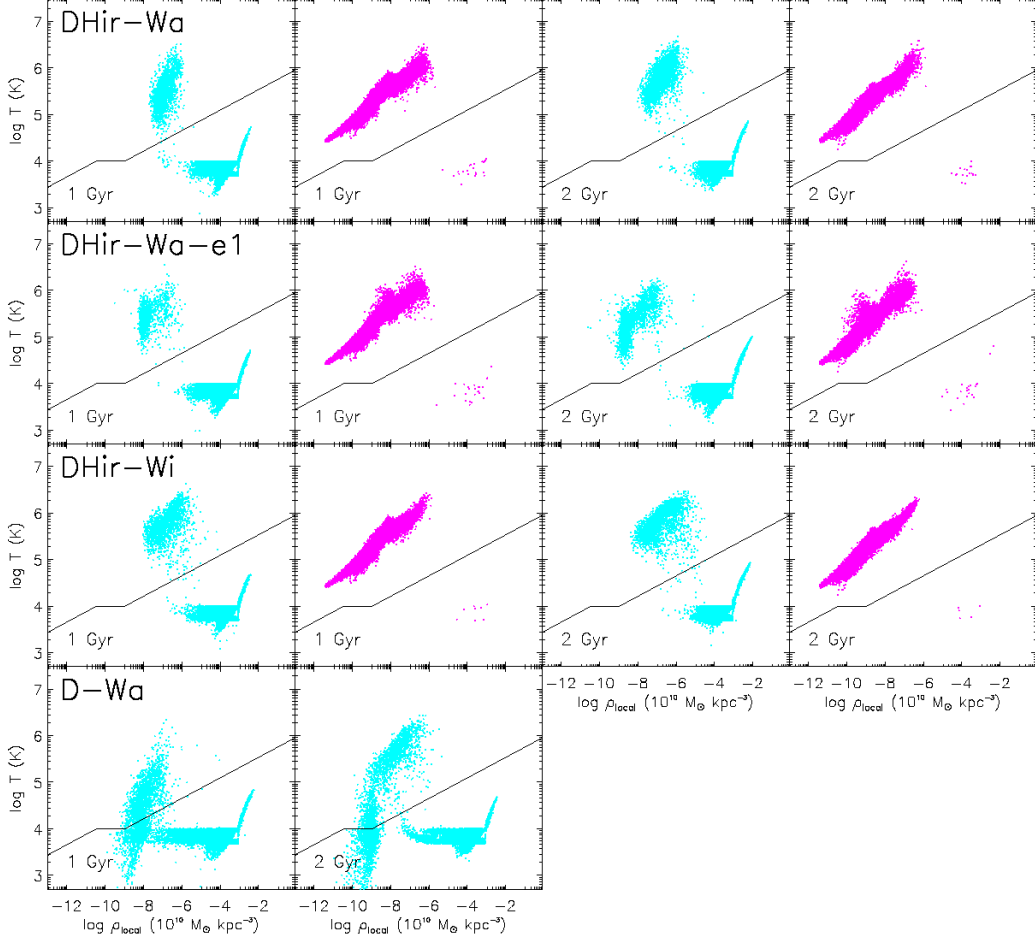


FIG. 12.— Temperature versus local density plots for the disk and halo gas of the wind test runs listed in Table 3. As same as Fig. 3, the cyan and magenta dots indicate the gas particles originally from the disk and halo, respectively, and the identical black line is used to distinguish the disk and halo gas at later times. Each row presents the plots from each run at $t = 1$ and 2 Gyr. The plots at the initial time are not shown here since they are the same as those of either model DHir or model D in Fig. 3. More gas particles crossing the black line upwardly are seen due to the wind effects compared to the runs without winds.

winds, run D-Wa accounts for galactic winds throughout the simulation. Axial winds with the wind efficiency $\eta = 2$ are chosen in this run as in run DHir-Wa (Table 3).

The snapshots of run D-Wa at $t = 0.1, 0.5, 1$, and 2 Gyr are presented in Fig. 17. Compared to run D without winds, fewer number of stars are added onto the star disk from the gas disk (blue dots; also refer to $N_{\text{ds,d2s}}$ in Table 4). The gas flow caused by the winds is seen as a bipolar pattern in the snapshots. Some of the gas particles ejected from the plane of the gas disk are classified as the gas disk particles in the snapshots, and the others as the gas halo particles (cyan circles), according to the T - ρ_{local} criterion. At later times, most of the ejected particles are defined as the halo gas. The T - ρ_{local} diagrams (bottom row in Fig. 12) show that some of the gas particles originally set as the gas disk are located above the criterion line due to the wind effects; this is in contrast to the case of run D where no gas particles cross the black line. As in the other runs with winds, the winds prevent gas particles from gathering at the center resulting in the smaller surface density at the center of the disk compared to run D, as seen in Fig. 13. The total mass of the star disk increases from the initial value $M_{\text{ds}} = 4.399 \times 10^{10} M_{\odot}$ to $M_{\text{ds}} = 4.455 \times 10^{10} M_{\odot}$ at $t =$

2 Gyr (Table 4), and that of the gas disk decreases from the initial value $M_{\text{dg}} = 0.6 \times 10^{10} M_{\odot}$ to $M_{\text{ds}} = 0.4824 \times 10^{10} M_{\odot}$ at $t = 2$ Gyr. The number of the gas halo particles at $t = 2$ Gyr is $N_{\text{hg}} = 2071$.

3.4. Star Formation History

Fig. 18 shows the SFRs of all of our simulations for 3 Gyr. The left column is for the runs without winds, and the right column is for the wind test runs.

In run D, where the galaxy model starts with a single gas component of the gas disk and does not account for the effects of galactic winds, the SFR (bottom-left panel) increases at the beginning for about half Gyr and decreases continuously afterwards. The maximum rate is $1.14 M_{\odot} \text{ yr}^{-1}$ at 0.36 Gyr. The star formation decreases afterwards because the cold and dense gas becomes less available as they are continually consumed by star formation (refer to Table 4). In run Hi, where the initial galaxy model has only a hot gas halo, the SFR is zero during the entire run.

The SFRs in the runs of type DH models without winds (top to fifth panels in the left column), where the galaxy models are initialized with both gas disk and gas halo, come out quite differently from that of run D without

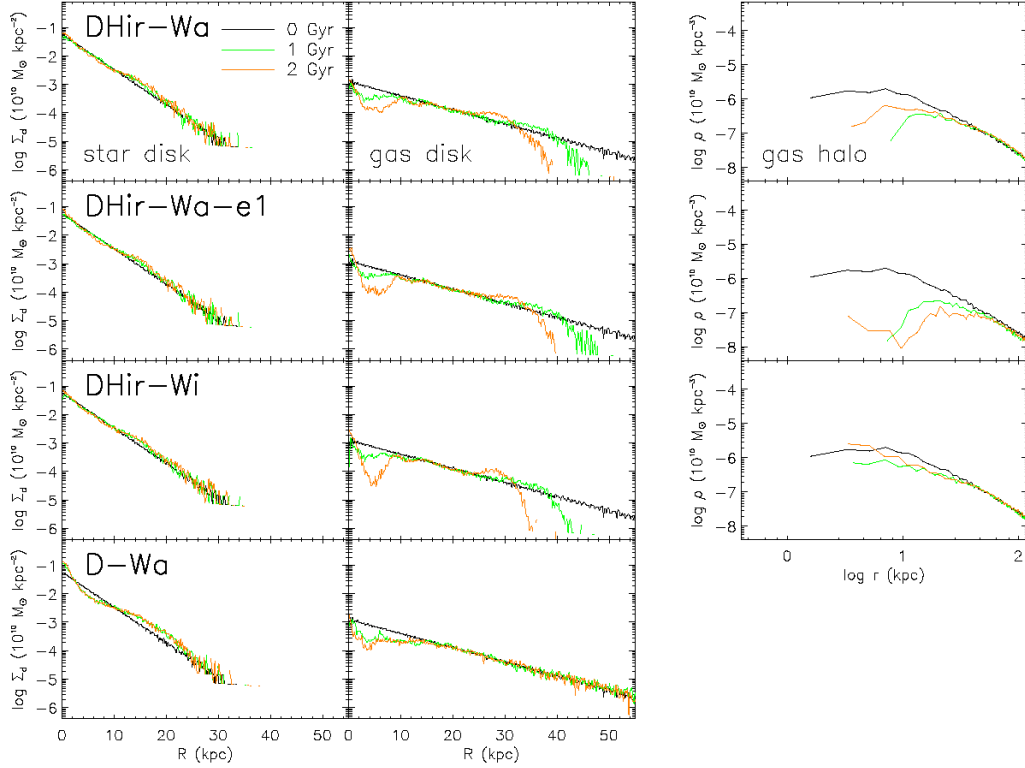


FIG. 13.— The surface and spherically averaged density profiles of the wind test runs at $t = 0, 1$, and 2 Gyr. As same as Fig. 4, the left to right columns present the surface density profiles of the star and gas disks, and the spherically averaged accumulated density profiles of the gas halos. Each row shows the profiles from each run.

a gas halo. In the fiducial run DHi (with an isothermal gas halo of $f_{\text{gh}}=0.01$), the SFR does not change much throughout the simulation. The rate reaches $0.837 \text{ M}_{\odot} \text{ yr}^{-1}$ at 0.024 Gyr, decreases slowly to $0.468 \text{ M}_{\odot} \text{ yr}^{-1}$ at 0.91 Gyr, and increases again to $0.745 \text{ M}_{\odot} \text{ yr}^{-1}$ at 1.49 Gyr. The SFR is kept above $0.65 \text{ M}_{\odot} \text{ yr}^{-1}$ until about 2 Gyr and decreases afterwards. Compared with run D, the SFR in the fiducial run is lower for about the first 1 Gyr. However, the SFR becomes higher during the last 2 Gyr than in run D. Most of the new stars in this run are generated from the gas originating from the gas disk (Table 4).

In run DHi-f5 (with a more massive isothermal gas halo of $f_{\text{gh}}=0.05$), the SFR is higher than in the run with the fiducial model DHi at all times. The SFR in run DHi-f5 increases steeply to the maximum rate $2.658 \text{ M}_{\odot} \text{ yr}^{-1}$ at 1.48 Gyr and decreases later to $0.9 \text{ M}_{\odot} \text{ yr}^{-1}$ at the end of the run. The maximum rate is about three times greater than that in the fiducial run. The time when the rate reaches its maximum is affected by the adopted value of the model parameter for star formation time-scale $t_0^* = 1.47$ Gyr. Star formation occurs mostly in the gas originally set as the gas disk and only a few percent of the stars are formed out of the initially halo gas (Table 4).

The SFR in run DHir (with a rotating isothermal gas halo of $f_{\text{gh}}=0.01$) is maintained relatively constant throughout the simulation than in all the other runs. The SFR is very close to that in the fiducial run DHi (with the same but non-rotating gas halo) for the first 1 Gyr but gets lower in the middle of the run from ~ 1 Gyr to ~ 2.5 Gyr by up to $\sim 0.2 \text{ M}_{\odot} \text{ yr}^{-1}$. As listed in Table 4,

the number of stars generated from the gas initially set as the gas disk is smaller than that in the fiducial run at each time; the number of new stars from the gas originally from the gas halo is a few times larger, however their total mass is still insignificant as $\lesssim 1\%$ of the total mass of all new stars. It is implied that the rotation of the gas halo in this run helps some halo gas particles to be accreted down to the gas disk more easily, however, it affects overall to lower star formation activity than in the run without the initial rotation.

In run DHn (with a NFW gas halo of $f_{\text{gh}}=0.01$), the SFR is much higher than that in the fiducial run DHi at all times due to the more centrally concentrated NFW gas halo. The SFR in run DHn is rather more comparable to that in run DHi-f5 than in run DHi, although the maximum rate $1.866 \text{ M}_{\odot} \text{ yr}^{-1}$ at 1.72 Gyr is certainly lower than in run DHi-f5. The percentage of the stars formed out of the gas originating from the gas halo becomes significant in run DHn; it is a few times greater than that in run DHi-f5 (Table 4).

In run DHn-f5 (with a massive NFW gas halo of $f_{\text{gh}}=0.05$), the SFR is higher than in all the other runs throughout the simulation. The SFR increases very rapidly from the start of the run over $5.5 \text{ M}_{\odot} \text{ yr}^{-1}$ in 0.35 Gyr, and reaches the maximum rate 6.94 at 1.66 Gyr. After the maximum, it decreases rapidly to $2.960 \text{ M}_{\odot} \text{ yr}^{-1}$ at 2.47 Gyr and slows down till the end of the run. The amount of new stars generated from the halo gas at later times is comparable to that from the disk gas, as the gas set as the gas disk are largely consumed by the times while a significant number of gas particles from the centrally concentrated massive gas halo are still

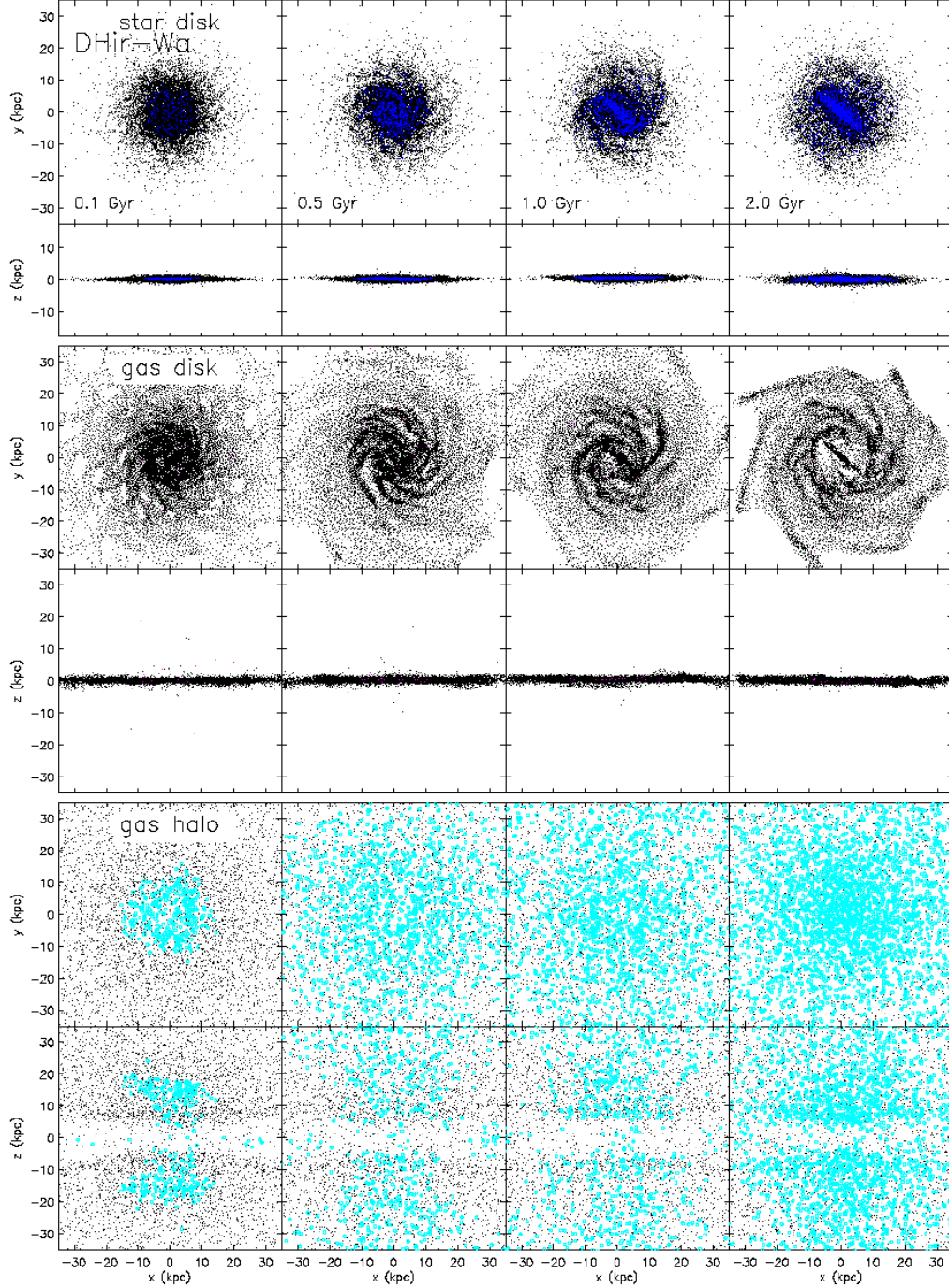


FIG. 14.— Four snapshots from run DHir-Wa which includes axial galactic winds associated with star formation during the simulation. These snapshots are taken at the same times as those in Figs 5 through 11 and the colors are also used in the same way. Compared to the runs without winds, the star disk tends to have less number of newly formed stars (blue and red dots). Some gas particles are ejected from the plane of the disk by the stellar winds out to several tens of kpc; those ejected and heated gas are seen in the bottom two rows (cyan circles).

cooled down to the gas disk (Table 4).

In the wind test runs, the SFRs come out always lower than those in the corresponding runs without winds, because the winds disturb cold gas from being concentrated. Including axial winds with the wind efficiency $\eta = 2$, the SFR in run D-Wa (bottom-right) has its maximum $0.91 \text{ M}_{\odot} \text{ yr}^{-1}$ at 0.13 Gyr, which is $0.23 \text{ M}_{\odot} \text{ yr}^{-1}$ less than the maximum rate in run D. After the max-

imum, the SFR decreases more rapidly than in run D down to $0.147 \text{ M}_{\odot} \text{ yr}^{-1}$ at 1 Gyr and 0.022 at 3 Gyr. In run DHir-Wa with axial winds and the efficiency $\eta = 2$, the SFR is also lower than in run DHir without winds. With the reduced wind efficiency $\eta = 1$ in run DHir-Wa-e1, the SFR becomes overall higher than that in run DHir-Wa and lower than that in run DHir. In run DHir-Wi adopting isotropic winds with the wind

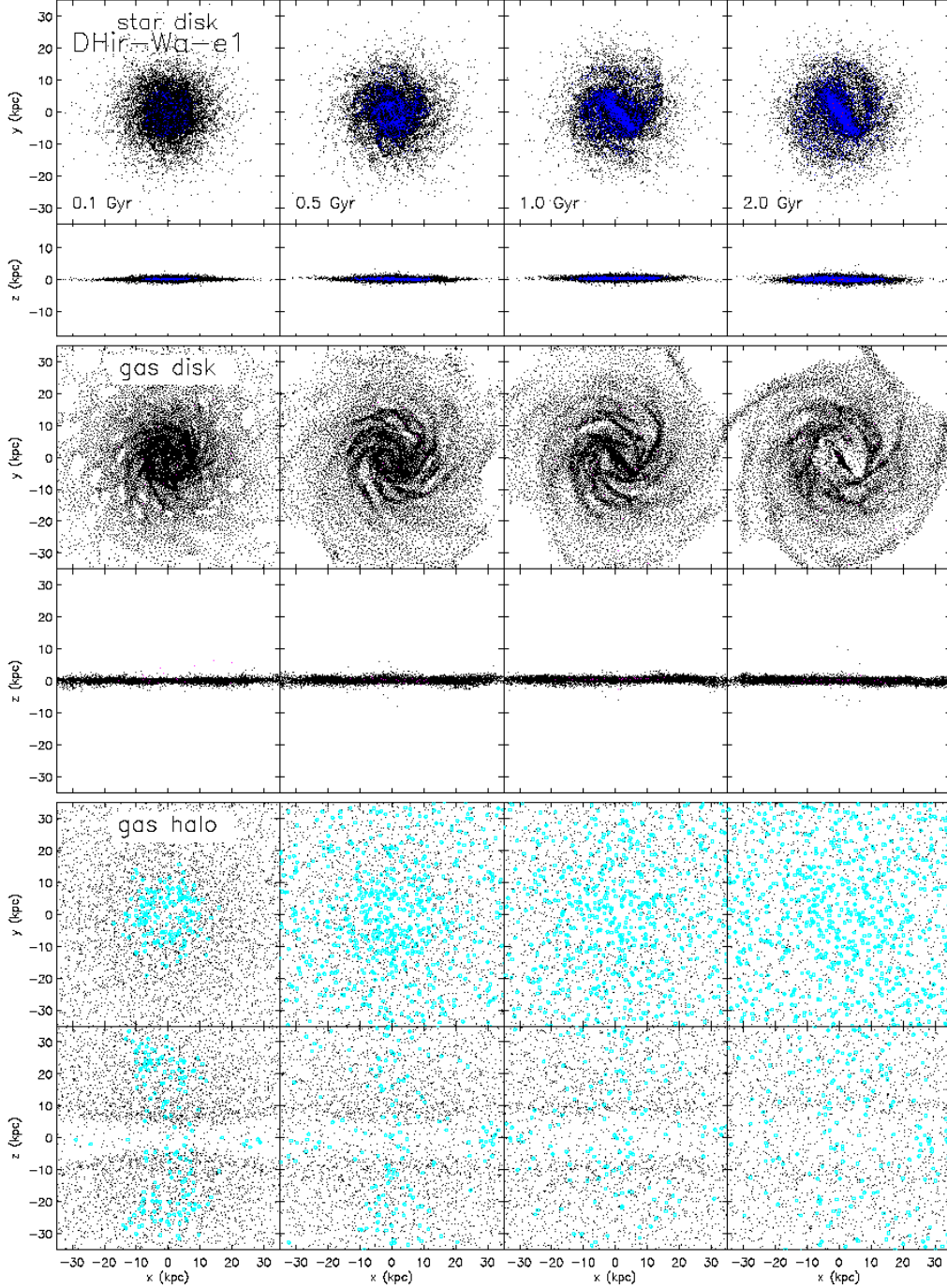


FIG. 15.— The same snapshots as Fig. 14, but from run DHir-Wa-el. As the previous run DHir-Wa, this run includes axial galactic winds but with a half the wind efficiency.

efficiency $\eta = 2$, the SFR comes out close to that in run DHir-Wa with axial winds.

4. SUMMARY AND DISCUSSION

Motivated by the existence of hot gaseous halo in spiral galaxies evidenced by both observations and simulations, we have investigated the effects of a gas halo on the evolution of isolated Milky Way-like galaxies using N -body/Hydrodynamic simulations. We have also examined the effects of galactic winds driven by supernovae on the evolution.

To generate the initial galaxy models, we used the ZENO software package. We built seven different galaxy models, with or without a gas halo component with varying mass and density profile for comparison (Tables 1 and 2): We tried two different density profiles for the gas halo - an isothermal profile and an NFW profile. We also tested different amounts of the halo gas fraction - $f_{\text{hg}} = 0.01$ and $f_{\text{hg}} = 0.05$. In addition, we studied a case with an initially rotating gas halo. We set the disk gas fraction $f_{\text{dg}} = 0.12$ equally in all models possessing a gas disk.

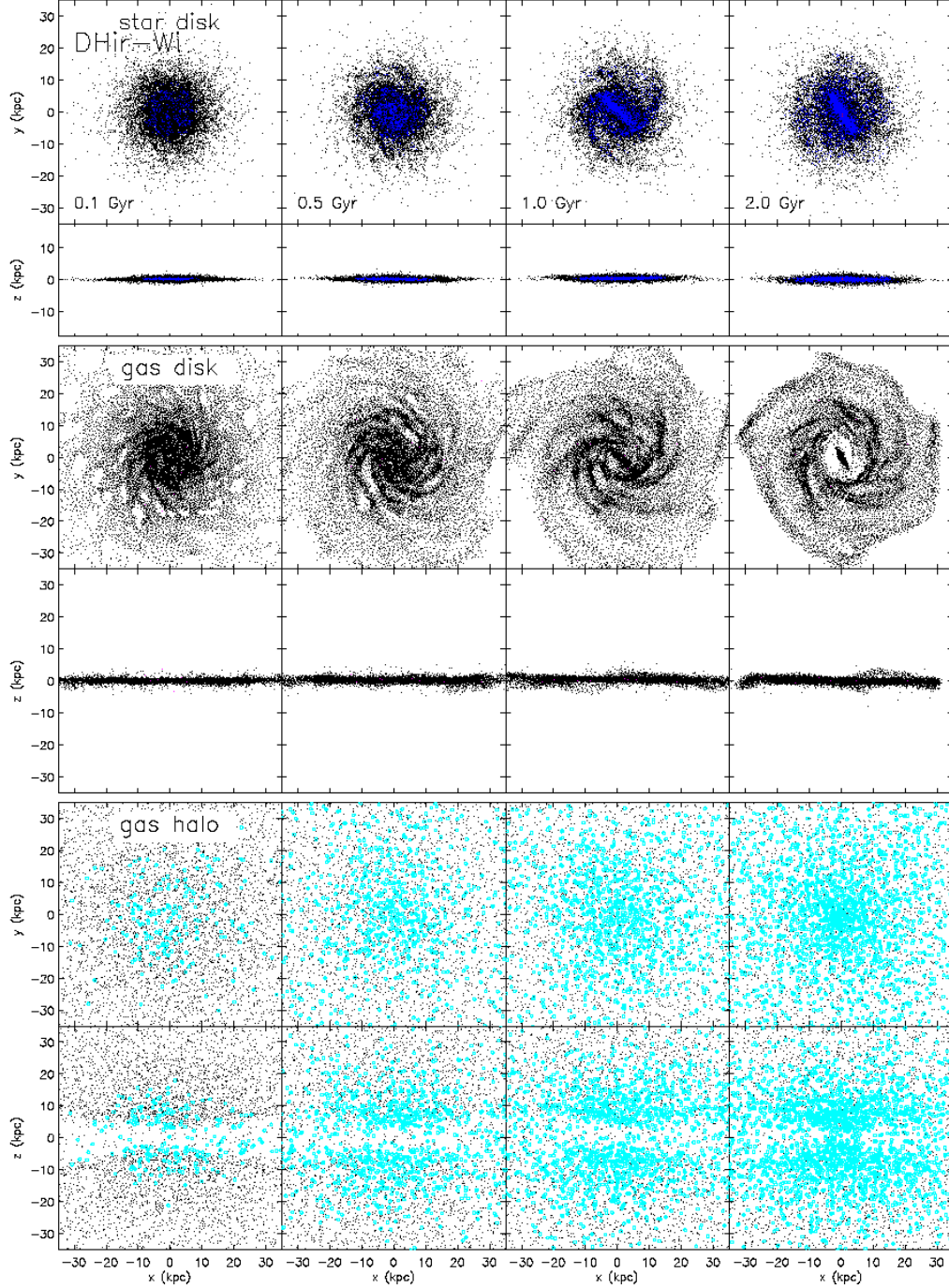


FIG. 16.— The same snapshots as Fig. 14, but from run DHir-Wi which includes isotropic galactic winds.

Each galaxy model was then evolved in isolation using the N -body/SPH code GADGET-3 (an early version), first without including stellar winds driven by star formation. The effects of winds are also studied. In the wind test runs, either axial winds or isotropic winds were tested, with the wind efficiency of either $\eta = 2$ or $\eta = 1$.

We showed that the effects of the hot gas component on the evolution are significant, particularly in the gas disk dissipation/accretion and in the star formation activity. The runs with a gas halo show higher SFRs in the middle to last phase of the 3 Gyr-simulations than in the

run without a gas halo where the SFR reaches its maximum at the early phase and then decreases continuously thereafter. The star formation activity in the disks is affected by both the mass concentration at the inner part and the total mass of the gas halo. The more centrally concentrated NFW gas halo leads higher SFRs than in runs with the isothermal gas halo of the same total mass. In runs where the gas halo has higher density at the central halo and/or greater total mass, the SFRs are higher than others and the gas disks dissipate too quickly. The gas accretion from the halo onto the disk in those runs

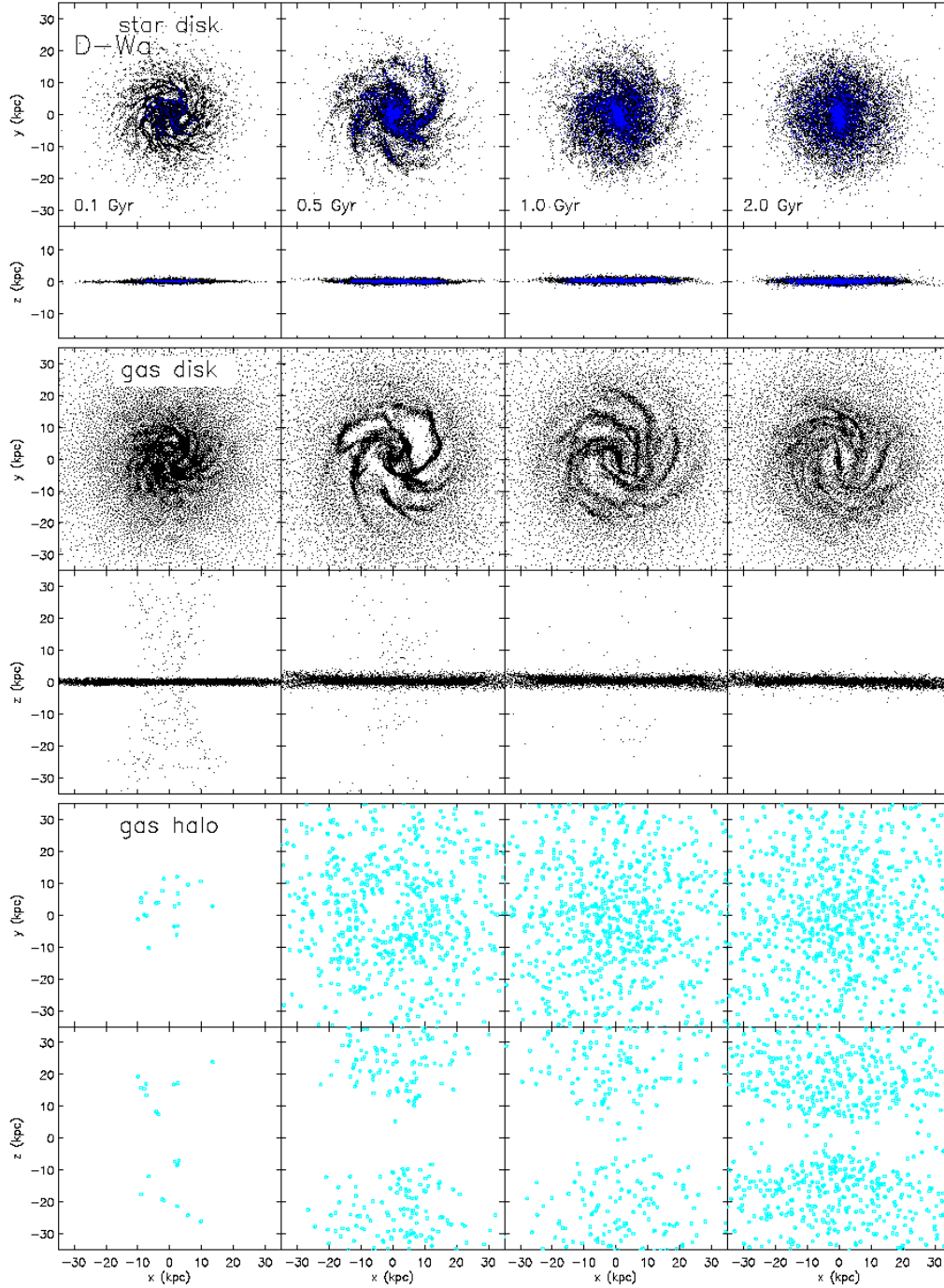


FIG. 17.— The same snapshots as Fig. 14, but from run D-Wa which includes axial galactic winds.

turns out to occur not much actively, and some portion of the accreted gas are quickly consumed by star formation as well, resulting in unrealistically small gas disks after a few Gyr. It is not clear which physical processes are mainly responsible for the dissipation of gas disks.

Models DHi (the fiducial model) and DHir (with the additional rotation of the gas halo to the fiducial model) show relatively reasonable results in both the gas dissipation and the star formation activity. The SFR in run DHi is a bit higher than that in run DHir in the middle of the evolution. The mass of the gas disk is slightly greater in

run DHir. It turned out that the initial rotation of the gas halo leads more gas accretion from the halo to the disk but delays the star formation activity in the disk. The specific mechanism of how the rotation hinders star formation, however, needs to be further investigated.

With model DHir and model D we performed four more simulations including supernova-driven galactic winds. In these wind test runs, the SFRs come out lower than the corresponding runs without winds at all times as expected. Both axial and isotropic winds result in overall similar SFRs. The run with the reduced wind efficiency

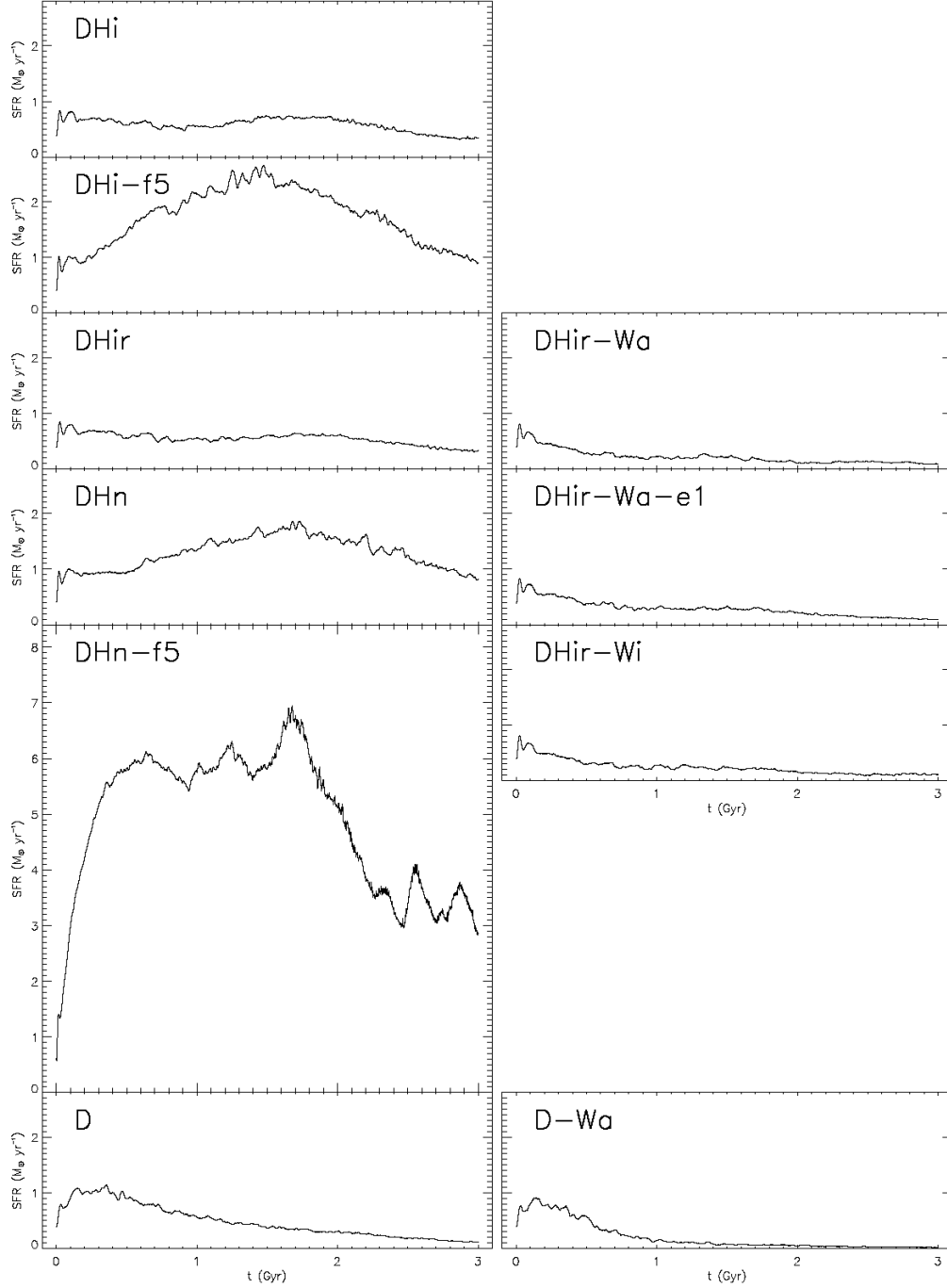


FIG. 18.— SFRs over the course of simulations. The left and right columns show the rate from the runs without winds and with winds, respectively. Run Hi is not shown as it has zero star formation throughout the simulation.

shows higher SFR than that with the default value of the wind efficiency.

In our initial galaxy models, we kept the total mass of the system as well as the total masses of the halo (DM + gas), disk (stars + gas), and bulge components equally to focus on examining the impacts of the different gas distribution and rotation of the gas halo. Our simulation results, such as in the gas dissipation and accretion and the star formation activities, are restricted by our initial galaxy models and the parameter values in the simulation code. The wind effects would also be affected by a variety

of factors, for instance the total mass of the galaxy model, and be limited by the provided wind model in the code.

Nonetheless, numerical studies to seek more realistic galaxy models including a gas halo component are demanded since the component as a large reservoir of gas influences the evolution of the galaxies. Adding a gas halo in numerical simulations, various gas dynamical processes that may occur in real systems both isolated or interacting with others, would be better interpreted.

The galaxy models are eventually compared with the ‘galaxies’ in cosmological simulations (Kim et al. 2011).

We plan to use our isolated galaxy models to understand the morphology and luminosity transformation of interacting galaxies (Park et al. 2008) found in the Sloan Digital Sky Survey (Choi et al. 2010).

We are grateful to Joshua E. Barnes and Volker

Springel for offering the ZENO package and the GADGET code, respectively. J.-S. H. thanks Walter Dehnen, Juhan Kim, and Maurice H. P. M. van Putten for helpful discussions. We thank the Korea Institute for Advanced Study for providing computing resources (KIAS Center for Advanced Computation Linux Cluster System) for this work.

APPENDIX

A. Construction of initial galaxy models with ZENO

Here we describe the procedure for constructing the models possessing both gas disk and gas halo and then disk-only or halo-only models, using several programs provided in the ZENO package (c.f. Barnes & Hibbard 2009).

To construct the N -body realization of the spherical components of the models of type DH, we first obtain the cumulative mass profiles of each component by integrating the corresponding mass density profiles with the parameter values shown in Table 4.

For the bulge, we use the program *gammagsp* in the ZENO package. This code generates profiles for Dehnen models (Dehnen 1993), including the Hernquist profile (Eq. 4) with $\gamma = 1$ in the input options. We truncate the mass distribution of the bulge from the radius b_b as indicated in Eq. 4 and rescale to the original mass, using the program *gsprun*. For the profile of either DM or gas halo following the NFW model (Eq. 2), we run *halogsp*. The profile of the gas halo following the non-singular isothermal form (Eq. 3; type DHi) is generated by *isothgsp*. The total spheroid mass profile and the total mass profile are calculated in accordance with the choice of the halo profile. The disk is represented by an infinitely thin disk at this stage (see Barnes & Hibbard 2009 for detail), and the profile of the ‘spherical’ (infinitely thin) disk is generated by *expdgsp*. We then combine the mass profiles of the bulge, the DM and the gas halos, and the ‘spherical’ disk to get the total cumulative mass profile using *gsppadd*, and smooth the profile using *gspsmooth*. Finally, we generate each of the spherical components, running two N -body realization codes, *gsprealize* for the bulge and the DM halo and *gspsphere* for the gas halo, with the input parameters of the density profile of the component as well as the smoothed total mass profile for the gravity calculation. The *gsprealize* code uses the Abel integral to compute the distribution function and generates a configuration of the body in phase-space. The *gspsphere* code outputs the initial positions and internal energies of the halo gas particles with zero initial velocities.

To make realizations of the star and the gas disks we run *gsdisk* twice. This code makes an exponential disk embedded in the smoothed total spheroid mass profile with the disk mass and other parameters given in Table 4. For the initial velocities of the star disk particles, the local circular velocities and the vertical and radial dispersions are calculated in the way described in Barnes & Hibbard 2009. For the gas particles, we set zero dispersion.

The procedure for making model DHir (disk plus halo model with rotation) is the same as in model DHi (the fiducial model), except an additional step for giving rotation of the gas halo using a simple code we made. We set the rotation such that the gas halo has the rotation curve with a similar shape but half the amplitude of that of the disk.

To build either the disk-only model (model D) or the halo-only model (model Hi), one can follow the steps described above but skipping the parts related to either the gas halo or the gas disk, respectively.

B. Long-term evolution of model DHir

Fig. 19 shows four more snapshots from run DHir at later times since those in Fig. 7. More stars are seen in the star disk than in Fig. 7. The inner part of the gas disk appears largely dissipated as time passes, and the refilling of the gas disk by accreting halo gas does not seem to occur actively.

The total mass of the star disk increases to $M_{ds} = 4.56 \times 10^{10} M_\odot$ at $t = 3$ Gyr, and $4.59 \times 10^{10} M_\odot$ at $t = 5$ Gyr. Among the stars in the disk at $t = 3$ Gyr, the number of stars added from the gas originally set as the gas disk and the gas halo are $N_{ds,d2s} = 8600$ (blue dots in the first two rows) and $N_{ds,h2s} = 94$ (red dots), respectively. The total mass of the gas disk decreases to $M_{dg} = 0.44 \times 10^{10} M_\odot$ at $t = 3$ Gyr, and $0.41 \times 10^{10} M_\odot$ at $t = 5$ Gyr. The total mass of the gas halo is maintained to $M_{hg} = 1.2 \times 10^{10} M_\odot$ at $t = 3$ and 5 Gyr.

REFERENCES

- Anderson, M. E., & Bregman, J. N. 2010, Do Hot Halos Around Galaxies Contain the Missing Baryons?, *ApJ*, 714, 320
- Barnes, J. E., & Hernquist, L. 1992, Dynamics of Interacting Galaxies, *ARA&A*, 30, 705
- Barnes, J. E., & Hibbard, J. E. 2009, Identikit 1: A Modeling Tool for Interacting Disk Galaxies, *AJ*, 137, 3071
- Blumenthal, G. R., Faber, S. M., Primack, J. R., & Rees, M. J. 1984, Formation of Galaxies and Large-Scale Structure with Cold Dark Matter, *Nature*, 311, 517
- Choi, J.-H., & Nagamine, K. 2011, Multicomponent and Variable Velocity Galactic Outflow in Cosmological Hydrodynamic Simulations, *MNRAS*, 410, 2579
- Choi, Y.-Y., Han, D.-H., & Kim, S. S. 2010, Korea Institute for Advanced Study Value-Added Galaxy Catalog, *JKAS*, 43, 191
- Dehnen, W. 1993, A Family of Potential-Density Pairs for Spherical Galaxies and Bulges, *MNRAS*, 265, 250
- Dekel, A., & Silk, J. 1986, The Origin of Dwarf Galaxies, Cold Dark Matter, and Biased Galaxy Formation, *ApJ*, 303, 39
- Deng, X.-F., Zhang, F., Song, J., Chen, Y.-Q., & Jiang, P. 2012, The Environmental Dependence of the Fraction of ‘Unconventional’ Galaxies: Faint Red and Luminous Blue, *JKAS*, 45, 59
- Hernquist, L. 1990, An Analytical Model for Spherical Galaxies and Bulges, *ApJ*, 356, 359
- Hernquist, L. 1993, N -body Realizations of Compound Galaxies, *ApJS*, 86, 389
- Hopkins, P. F., Quataert, E., & Murray, N. 2011, Self-Regulated Star Formation in Galaxies via Momentum Input from Massive Stars, *MNRAS*, 417, 950
- Hwang, H. S., & Park, C. 2009, Evidence for Morphology and Luminosity Transformation of Galaxies at High Redshifts, *ApJ*, 700, 791

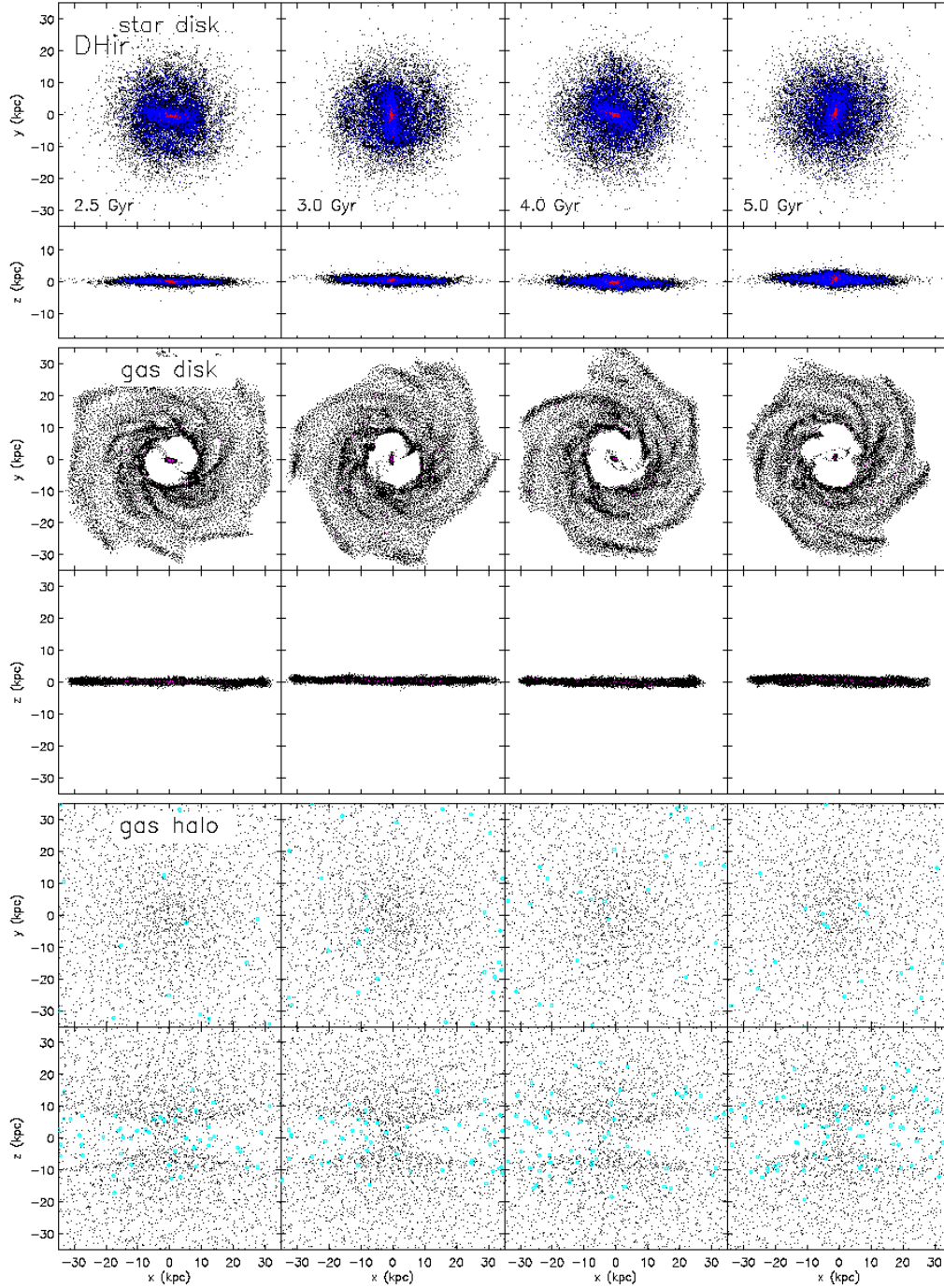


FIG. 19.— The particle distribution of run DHir without winds after the time shown in Fig. 7. The first to fourth columns show the snapshots at $t = 2.5, 3, 4$, and 5 Gyr, respectively.

Katz, N., Weinberg, D. H., & Hernquist, L. 1996, Cosmological Simulations with TreeSPH, *ApJS*, 105, 19
 Kazantzidis, S., Magorrian, J., & Moore, B. 2004, Generating Equilibrium Dark Matter Halos: Inadequacies of the Local Maxwellian Approximation, *ApJ*, 601, 37
 Kennicutt, R. C. Jr. 1998, The Global Schmidt Law in Star-Forming Galaxies, *ApJ*, 498, 541
 Kim, J., Park, C., Rossi, G., Lee, S. M., & Gott, J. R. 2011, The New Horizon Run Cosmological N -Body Simulations, *JKAS*, 44, 217
 McKee, C. F., & Ostriker, J. P. 1977, A Theory of the Interstellar Medium: Three Components Regulated by Supernova Explosions in an Inhomogeneous Substrate, *ApJ*, 218, 148
 McMillan, P. J., & Dehnen, W. 2007, Initial Conditions for Disc Galaxies, *MNRAS*, 378, 541

Merritt, D. 1985, Distribution Functions for Spherical Galaxies, *MNRAS*, 214, 25P
 Moster, B. P., Macciò, A. V., Somerville, R. S., Naab, T. & Cox, T. J. 2011, The Effects of a Hot Gaseous Halo in Galaxy Major Mergers, *MNRAS*, 415, 3750
 Moster, B. P., Macciò, A. V., Somerville, R. S., Naab, T. & Cox, T. J. 2012, The Effects of a Hot Gaseous Halo on Disc Thickening in Galaxy Minor Mergers, *MNRAS*, 423, 2045
 Navarro, J. F., Frenk, C. S., & White, S. D. M. 1996, The Structure of Cold Dark Matter Halos, *ApJ*, 462, 563
 Osipkov, L. P. 1979, Spherical Systems of Gravitating Bodies with an Ellipsoidal Velocity Distribution, *Pis'ma Astr. Zh.*, 5, 77
 Park, C., & Choi, Y.-Y. 2009, Combined Effects of Galaxy Interactions and Large-Scale Environment on Galaxy Properties, *ApJ*, 691, 1828

- Park, C., Gott, J. R., & Choi, Y.-Y. 2008, Transformation of Morphology and Luminosity Classes of the SDSS Galaxies, *ApJ*, 674, 784
- Park, C., & Hwang, H. S. 2009, Interactions of Galaxies in the Galaxy Cluster Environment, *ApJ*, 699, 1595
- Salpeter, E. E. 1955, The Luminosity Function and Stellar Evolution, *ApJ*, 121, 161
- Springel, V. 2005, The Cosmological Simulation Code GADGET-2, *MNRAS*, 364, 1105
- Springel, V., Di Matteo, T., & Hernquist, L. 2005, Modelling Feedback from Stars and Black Holes in Galaxy Mergers, *MNRAS*, 361, 776
- Springel, V., & Hernquist, L. 2002, Cosmological Smoothed Particle Hydrodynamics Simulations: The Entropy Equation, *MNRAS*, 333, 649
- Springel, V., & Hernquist, L. 2003, Cosmological Smoothed Particle Hydrodynamics Simulations: A Hybrid Multiphase Model for Star Formation, *MNRAS*, 339, 289
- Toomre, A., & Toomre, J. 1972, Galactic Bridges and Tails, *ApJ*, 178, 623